



Dark Photons in the Early Universe: From Thermal Production to Cosmological Constraints

Xun-Jie Xu ^a and Boting Zhou ^{a,b}

^a*Institute of High Energy Physics, Chinese Academy of Sciences, Beijing 100049, China*

^b*School of Physical Sciences, University of Chinese Academy of Sciences, Beijing 100049, China*

E-mail: xuxj@ihep.ac.cn, zhoubt@ihep.ac.cn

ABSTRACT: Dark photons, a generic class of light gauge bosons that interact with the Standard Model (SM) exclusively through kinetic mixing, arise naturally in many gauge extensions of the SM. Motivated by these theoretical considerations, we present a comprehensive analysis of their thermal production in the early universe. Our calculation covers a broad range of dark photon masses from 0.1 keV to 100 MeV and include inverse decay, annihilation, and semi-Compton processes. Wherever possible, we present analytical estimates of the production rates and yields, and verify their accuracy numerically. For dark photons lighter than twice the electron masses (around 1 MeV), we find that our analytical estimate of the freeze-in yield based on resonant production is very accurate, implying that off-resonance contributions can be neglected in practice. For heavy dark photons, although this conclusion no longer holds, we derive an interesting ratio, $4\pi e/27 \approx 0.14$, with e the coupling constant of QED, that can be used to estimate the relative importance of on- and off-resonance contributions. Finally, using the calculated abundance of dark photons in the early universe, we derive cosmological constraints on the dark photon mass and kinetic mixing. Compared with bounds from stellar cooling and supernovae, the cosmological constraints are most stringent in the mass range from 0.1 MeV to 6 MeV, within which kinetic mixing at the level of $10^{-12} \sim 10^{-10}$ can be probed.

Contents

1	Introduction	1
2	Lagrangian and Boltzmann equation	2
3	Thermal processes	4
3.1	Inverse decay	4
3.2	Annihilation and semi-Compton	5
3.3	High-mass-regime yield estimate	6
4	The medium effect	7
4.1	Basic formulism	8
4.2	Resonant production	9
4.3	Photon-dark photon oscillation	11
5	Evolution	13
6	Cosmological constraints	15
7	Conclusion	17
A	Lorentz-invariant phase space integral	18
B	Collision terms	19
B.1	Annihilation	20
B.2	Semi-Compton	22
C	The photon self-energy in the thermal bath	24

1 Introduction

Among a plethora of extensions of the Standard Model (SM), one of the most extensively studied cases is gauge extensions. The simplest gauge extension, introducing an extra gauged $U(1)$, has an interesting feature: the associated gauge boson can couple through a kinetic mixing term to the hypercharge gauge boson of the SM [1]. When the new gauge boson is light (well below the electroweak scale), the kinetic mixing gives rise to photon-like interactions with SM particles; that is, its effective couplings to SM particles are proportional to their electric charges, with a universal suppression set by the kinetic-mixing parameter. Widely referred to as the dark photon, this light, weakly-coupled gauge boson has drawn considerable attention due to its rich phenomenology—see Refs. [2–8] for

recent reviews—including potential connections with the dark matter problem of the SM, and has also motivated numerous laboratory searches [9–16].

Complementary to laboratory searches, cosmology provides a powerful avenue for probing dark photons through their observable imprints on the evolution of the early universe [17–33]. Depending on whether the mass is heavy (above the MeV scale) [19, 21, 23, 24], light (from keV to MeV) [17, 18, 27], or ultra-light (well below the aforementioned scales) [20, 22, 25, 26, 28–33], dark photons can be produced in multiple ways in the early universe. Heavy dark photons with kinematically-allowed decay channels to charged fermions can be efficiently produced via inverse decays from the thermal bath. Light dark photons are produced via scattering processes, which in certain regimes can be approximated by resonant conversion (or oscillation) between photons and dark photons. Ultra-light dark photons are often assumed to be produced non-thermally, e.g., via the misalignment mechanism.

In this work, we focus on the thermal production of dark photons in the early universe, which is essentially unavoidable in the thermal environment if the kinetic mixing is sizable. Although this has been computed in a few studies for various purposes (see, e.g., [17, 21, 24]), a consistent treatment applicable to both the heavy and light mass regimes is still lacking. Moreover, existing calculations require solving the Boltzmann equation numerically, whereas we attempt to push the analytical approach as far as possible. We show that, for both inverse decay and scattering processes, analytical collision terms can be obtained with sufficient accuracy for quantitative studies. In addition, the dark-photon yield in the freeze-in regime can also be estimated analytically. In particular, we derive an interesting ratio of resonant to post-resonance yields for heavy dark photons: $4\pi e/27 \approx 0.14$, where e is the QED coupling. This implies that, for heavy dark photons, resonant production provides a significant, though subdominant, contribution. We also apply our calculation to derive cosmological constraints on dark photons across a broad mass range, from 0.1 keV to 10 MeV. The constraints are derived with rather robust and conservative energy-density considerations, and we show that they are complementary to stellar cooling and supernovae bounds.

The structure of this paper is organized as follows. In Sec. 2, we introduce the basic formalism including the Lagrangian for the dark photon, its interactions, and the Boltzmann equation. In Sec. 3, we calculate the collision terms of relevant thermal processes, without including the medium effect (also known as the plasma effect), which is elaborated in Sec. 4. In Sec. 5, we discuss the evolution of dark photons and compare analytical results obtained in the previous sections with numerical solutions of the Boltzmann equation. Sec. 6 presents the cosmological constraints derived in this work. Finally, we conclude in Sec. 7 and relegate some details to the appendices.

2 Lagrangian and Boltzmann equation

In a gauged $U(1)$ extension of the SM, the gauge field associated with the extra $U(1)$ can couple to the gauge field of $U(1)_Y$ in the SM via the following kinetic mixing term [1]:

$$\mathcal{L} \supset -\frac{\epsilon}{2} F^{\mu\nu} F'_{\mu\nu}, \quad (2.1)$$

where ϵ is a coupling constant; and $F^{\mu\nu}$ and $F'_{\mu\nu}$ denote the field strength tensors of $U(1)_Y$ and the extra $U(1)$, respectively. After canonicalizing the kinetic terms and diagonalizing the mass terms of all gauge bosons (see, e.g., [34, 35]), one obtains gauge fields in mass eigenstates with properly normalized kinetic terms. Among the mass eigenstates, one should be massless due to the unbroken electromagnetic $U(1)$, and another can be relatively light compared with the electroweak scale. The former is identified as the photon (with the field denoted by A_μ and the particle by γ) whereas the latter is defined as the dark photon (with the field denoted by A'_μ and the particle by γ'). The mass of the dark photon, denoted by $m_{\gamma'}$, may arise from spontaneous symmetry breaking of the extra $U(1)$ [19, 34] or the Stückelberg mechanism [36, 37].

The canonicalization of kinetic terms gives rise to interactions of A and A' with SM fermions:

$$\mathcal{L} \supset e J_{\text{em}}^\mu (A_\mu + \epsilon A'_\mu), \quad (2.2)$$

where $e = \sqrt{4\pi\alpha}$ with $\alpha \approx 1/137$ the fine structure constant, J_{em}^μ is the electric current, and $\epsilon = \epsilon \cos \theta_W$ with θ_W the Weinberg angle. We note here that in the basis of mass eigenstates, the kinetic mixing has been removed and A' interacts with the SM only via Eq. (2.2).

In the early universe, the dark photon can be produced through particle scattering processes in the thermal bath, and can also be absorbed through the corresponding inverse processes. Its phase space distribution function, denoted by $f_{\gamma'}(t, p)$, obey the Boltzmann equation:

$$\left[\frac{\partial}{\partial t} - H p \frac{\partial}{\partial p} \right] f_{\gamma'}(t, p) = \Gamma_{\gamma'}^{\text{gain}} (1 + f_{\gamma'}) - \Gamma_{\gamma'}^{\text{loss}} f_{\gamma'}, \quad (2.3)$$

where $H = \dot{a}/a$ is the Hubble parameter with a the scale factor, and $\Gamma_{\gamma'}^{\text{gain/loss}}$ denotes the gain or loss rate of γ' due to dark photon interactions. In the radiation-dominated era, the Hubble parameter is given by

$$H = g_H \frac{T^2}{m_{\text{pl}}}, \text{ with } g_H \equiv 1.66 g_\star^{1/2}. \quad (2.4)$$

Here, T is the temperature of the thermal bath, $m_{\text{pl}} \approx 1.22 \times 10^{19}$ GeV is the Planck mass, and g_\star denotes the effective number of relativistic degrees of freedom.

When $f_{\gamma'} \ll 1$, corresponding to the freeze-in regime, one may neglect the backreaction term $\Gamma_{\gamma'}^{\text{loss}} f_{\gamma'}$ in Eq. (2.3) and write it in the following integral form:

$$f_{\gamma'}(a, p) \approx \int_0^a \frac{\Gamma_{\gamma'}^{\text{gain}}(a', ap/a')}{H(a')a'} da'. \quad (2.5)$$

Here, $f_{\gamma'}$ and $\Gamma_{\gamma'}^{\text{gain}}$ have been re-defined as functions of a and p , i.e., $f_{\gamma'} = f_{\gamma'}(a, p)$ and $\Gamma_{\gamma'}^{\text{gain}} = \Gamma_{\gamma'}^{\text{gain}}(a, p)$. Equation (2.5) is derived through a change of variables from t to a and p to the comoving momentum—see, e.g., Appendix B of Ref. [38] for a detailed derivation.

In this work, we also consider the number density of γ' , denoted $n_{\gamma'}$, which satisfies the following Boltzmann equation:

$$\frac{dn_{\gamma'}}{dt} + 3Hn_{\gamma'} = C_{\gamma'}^{\text{gain}} - C_{\gamma'}^{\text{loss}}, \quad (2.6)$$

where the collision terms $C_{\gamma'}^{\text{gain}}$ and $C_{\gamma'}^{\text{loss}}$ are the phase space integrals of the gain and loss terms in Eq. (2.3), respectively. Similar to Eq. (2.5), one can derive an integral form for $n_{\gamma'}$ in the freeze-in regime:

$$n_{\gamma'} a^3 \approx \int_0^a \frac{a'^2 C_{\gamma'}^{\text{gain}}(a')}{H(a')} da', \quad (2.7)$$

with

$$C_{\gamma'}^{\text{gain}} \approx \int g_{\gamma'} \frac{d^3 p}{(2\pi)^3} \Gamma_{\gamma'}^{\text{gain}}. \quad (2.8)$$

Here $g_{\gamma'}$ denotes the number of degrees of freedom of γ' .

Throughout this paper, we often divide $n_{\gamma'}$ by the entropy density

$$s = g_{\star,s} \frac{2\pi^2 T^3}{45}, \quad (2.9)$$

where $g_{\star,s}$ is the effective number of relativistic degrees of freedom in entropy. In the absence of interactions (or when production and deletion processes are inactive), $n_{\gamma'}/s$ is approximately constant.

3 Thermal processes

We consider dark photon thermal production in the early universe when it is dominated by photons (γ), electrons (e^\pm) and neutrinos ($\nu/\bar{\nu}$), corresponding to an epoch of $1 \text{ eV} \lesssim T \lesssim 100 \text{ MeV}$. Below $\sim 1 \text{ eV}$, the universe undergoes matter-radiation equality (0.8 eV) and recombination (0.3 eV), which are not included in our analysis. Above $\sim 100 \text{ MeV}$, one needs to include more thermal species (μ^\pm , π^\pm , etc.) in the analysis while the corresponding yield of γ' produced at such temperatures is subdominant for light γ' . Hence for simplicity, we neglect this part.

During this epoch, dark photons are dominantly produced through thermal processes involving γ and e^\pm , including (i) inverse decay ($e^+ e^- \rightarrow \gamma'$), (ii) electron-positron annihilation ($e^+ e^- \rightarrow \gamma' \gamma$), and (iii) semi-Compton scattering ($\gamma e^\pm \rightarrow \gamma' e^\pm$), as shown in Fig. 1. The inverse decay process is kinematically allowed only when $m_{\gamma'} > 2m_e$. The annihilation process is Boltzmann suppressed when T drops below m_e . The semi-Compton process is less suppressed at low temperatures compared to annihilation, and becomes the most important process at $T \lesssim 20 \text{ keV}$, below which positrons almost disappear while a certain amount of electrons remain due to matter-antimatter asymmetry.

Below, we calculate the collision terms of these processes. For simplicity, we assume Boltzmann statistics, which is a common approximation used in collision term calculations.

3.1 Inverse decay

For the inverse decay process, $e^+ e^- \rightarrow \gamma'$, the gain rate of γ' reads

$$\Gamma_{e^+ e^- \rightarrow \gamma'}^{\text{gain}} = \frac{1}{2\omega} \int g_1 d\Pi_1 g_2 d\Pi_2 f_1 f_2 (2\pi\delta)^4 |\mathcal{M}|^2, \quad (3.1)$$

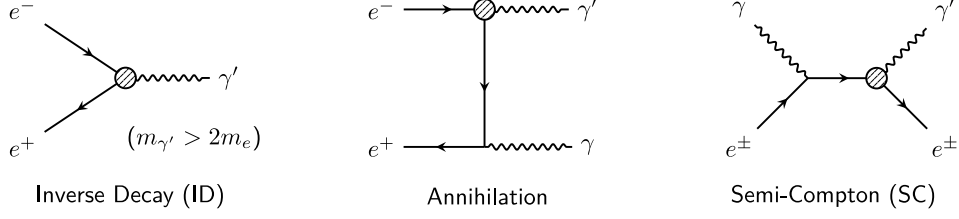


Figure 1. Thermal processes for dark photon production, including inverse decay (left), annihilation (middle), and semi-Compton (right). The hatched blobs indicate the effective coupling of γ' to electrons in thermal plasma.

where ω denotes the energy of γ' , $d\Pi_i = \frac{d^3 p_i}{(2\pi)^3 2E_i}$ with p_i and E_i the momentum and energy of the i -th particle in the considered process, $(2\pi\delta)^4$ is the common delta function responsible for momentum conservation, and $|\mathcal{M}|^2$ is the squared matrix element (with all spins and polarizations averaged out). The factor g_i accounts for the multiplicity of particle i , and f_i denotes its phase space distribution.

The squared matrix element of $e^+e^- \rightarrow \gamma'$ is given by

$$|\mathcal{M}|^2 = \frac{1}{g_{\gamma'} g_{e^+} g_{e^-}} 4e^2 \varepsilon^2 (m_{\gamma'}^2 + 2m_e^2), \quad (3.2)$$

where $g_{e^+} = g_{e^-} = 2$ account for the two degrees of freedom of spin. They will be canceled out by g_1 and g_2 in Eq. (3.1). Similarly, the multiplicity factor $g_{\gamma'}$ will eventually be canceled out by the $g_{\gamma'}$ factor in Eq. (2.8).

Since $|\mathcal{M}|^2$ in Eq. (3.2) is a constant, we may pull it outside the integral and perform the phase space integration straightforwardly. The technical details of computing such two-body phase space integrals are presented in Appendix A. The result reads

$$\Gamma_{e^+e^- \rightarrow \gamma'}^{\text{gain}} = \alpha \varepsilon^2 \frac{m_{\gamma'}^2 + 2m_e^2}{3\omega} \sqrt{1 - \frac{4m_e^2}{m_{\gamma'}^2}} e^{-\omega/T}. \quad (3.3)$$

Using Eq. (2.8), we obtain

$$C_{e^+e^- \rightarrow \gamma'}^{\text{gain}} = \alpha \varepsilon^2 \frac{m_{\gamma'}^2 + 2m_e^2}{2\pi^2} m_{\gamma'} T \sqrt{1 - \frac{4m_e^2}{m_{\gamma'}^2}} K_1\left(\frac{m_{\gamma'}}{T}\right), \quad (3.4)$$

where K_1 is the modified Bessel function. The above results are included in Tab. 1.

3.2 Annihilation and semi-Compton

For two-to-two processes like $e^+e^- \rightarrow \gamma\gamma'$ and $\gamma e^\pm \rightarrow e^\pm \gamma'$, it is generally difficult to work out the phase space integration analytically but, with certain approximations, we are able to derive analytical expressions—see Appendix B for the derivation and Tab. 1 for a summary of the results. On the other hand, using the Monte Carlo method described in Appendix B of [39], we also perform the integration numerically.

	$\Gamma_{\gamma'}^{\text{gain}}/\varepsilon^2$	$C_{\gamma'}^{\text{gain}}/\varepsilon^2$
$e^+e^- \rightarrow \gamma'$	$\alpha \frac{m_{\gamma'}^2 + 2m_e^2}{3\omega} \sqrt{1 - \frac{4m_e^2}{m_{\gamma'}^2}} e^{-\omega/T}$	$\alpha \frac{m_{\gamma'}^2 + 2m_e^2}{2\pi^2} m_{\gamma'} T \sqrt{1 - \frac{4m_e^2}{m_{\gamma'}^2}} K_1\left(\frac{m_{\gamma'}}{T}\right)$
$e^+e^- \rightarrow \gamma'\gamma$ ($T \gtrsim m_e$)	$\frac{\alpha^2 g_\Gamma T^2}{6\pi\omega} \left[\log\left(\frac{4T\omega}{m_e^2}\right) - \gamma_E - 1 \right] e^{-\frac{\omega}{T}}$	$\frac{\alpha^2 g_C T^4}{12\pi^3} \left[\log\left(\frac{4T^2}{m_e^2}\right) - 2\gamma_E \right]$
$e^+e^- \rightarrow \gamma'\gamma$ ($T \lesssim m_e$)	$\frac{\alpha^2 g_\Gamma T^{5/2}}{12\sqrt{\pi\omega} m_e} e^{-\frac{m_e^2 + \omega^2}{T\omega}}$	$\alpha^2 g_C \frac{4m_e^2 T^3 + 6m_e T^4 + 3T^5}{96\pi^2 m_e} e^{-\frac{2m_e}{T}}$
$\gamma e^\pm \rightarrow \gamma' e^\pm$ ($T \gtrsim m_e$)	$\frac{\alpha^2 g_\Gamma T^2}{12\pi\omega} \left[\log\left(\frac{4T\omega}{m_e^2}\right) - \gamma_E + \frac{1}{2} \right] e^{-\frac{\omega}{T}}$	$\frac{\alpha^2 g_C T^4}{12\pi^3} \left[\log\left(\frac{2T}{m_e}\right) - \gamma_E + \frac{3}{4} \right]$
$\gamma e^\pm \rightarrow \gamma' e^\pm$ ($T \lesssim m_e$)	$\frac{\sqrt{2}\alpha^2 g_\Gamma T^2}{9\sqrt{\pi T} m_e} \exp\left(\frac{\mu_{e^\pm} - m_e - \omega}{T}\right)$	$\frac{\sqrt{2}\alpha^2 g_C T^{9/2}}{9\pi^2 \sqrt{\pi m_e}} \exp\left(\frac{\mu_{e^\pm} - m_e}{T}\right)$

Table 1. Collision terms responsible for the production of γ' . For $e^+e^- \rightarrow \gamma'$, the presented expressions are exact. For $e^+e^- \rightarrow \gamma'\gamma$ and $\gamma e^\pm \rightarrow \gamma' e^\pm$, the expressions are derived with assumptions that high- T or low- T expansions are valid and $m_{\gamma'}$ is negligibly small. A few constants are defined as follows: $g_\Gamma \equiv g_e - g_{e^+} g_\gamma = 8$, $g_C \equiv g_e - g_{e^+} g_\gamma g_{\gamma'} = 24$, and γ_E is Euler's constant. The accuracy of these approximate expressions is demonstrated in Fig. 2.

In Fig. 2, we compare the analytical expressions with the Monte Carlo results. Here, the green and orange lines represent analytical expressions derived using the high- T and low- T approximations, respectively. These approximations are expected to be valid for $T \gg m_e$ or $T \ll m_e$, but in practice one can see that the resulting expressions remain accurate even when T is comparable to m_e . The comparison in Fig. 2 suggests that the high- T and low- T expressions can be matched to produce an expression that remains accurate across the full range, with the matching point set at $T = 2m_e$ for $e^+e^- \rightarrow \gamma\gamma'$, and $T = m_e$ for $\gamma e^\pm \rightarrow e^\pm \gamma'$.

It should be noted that when T is well below m_e , the electron-positron asymmetry becomes important, as it stops the electron number density from being further Boltzmann suppressed. At $T \lesssim 20$ keV, most positrons have annihilated with electrons while a residual population of electrons survives due to the asymmetry. Consequently, once the asymmetry becomes important, processes involving positrons effectively cease, and the production of γ' proceeds only through $\gamma e^- \rightarrow e^- \gamma'$. To include the asymmetry effect, we introduce chemical potentials μ_{e^\pm} for e^\pm in the last row of Tab. 1, i.e., the expressions with the low- T approximation of the semi-Compton process. For other collision terms, the asymmetry effect is negligible.

3.3 High-mass-regime yield estimate

When the dark photon is relatively heavy (compared with m_e), the dominant production channel is $e^+e^- \rightarrow \gamma'$, since $e^+e^- \rightarrow \gamma\gamma'$ and $\gamma e^\pm \rightarrow e^\pm \gamma'$ are suppressed by an extra power of α . Given the simplicity of the collision term $C_{e^+e^- \rightarrow \gamma'}^{\text{gain}}$, it is straightforward to plug it

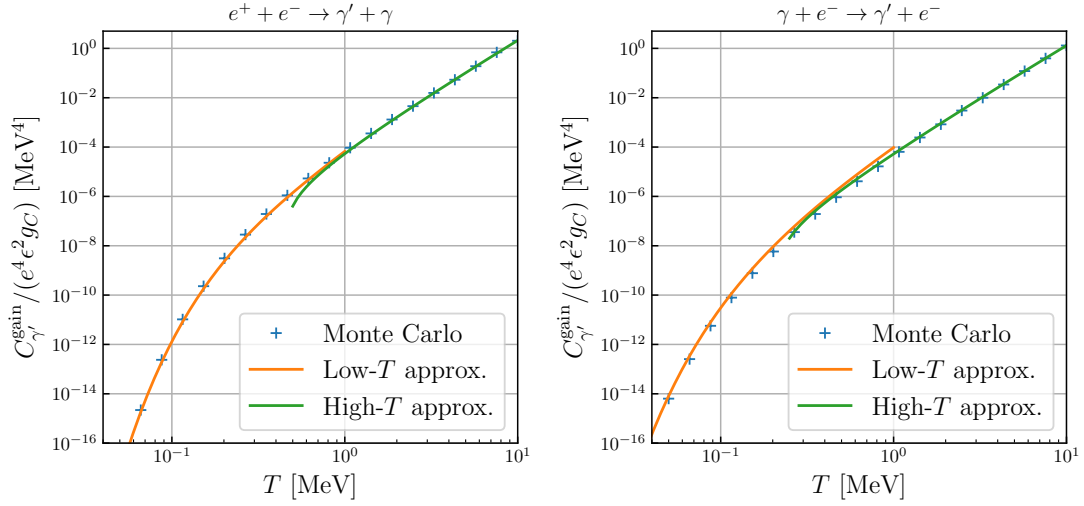


Figure 2. Comparison of the analytical expressions for two-to-two collision terms with Monte-Carlo results.

into Eq. (2.7) and obtain

$$\frac{n_{\gamma'}}{n_{\gamma}} \approx \frac{\pi \alpha \varepsilon^2 m_{\text{pl}}}{4 \zeta(3) g_H m_{\gamma'}} \frac{g_{\gamma'}}{g_{\gamma}} \left(1 + 2 \frac{m_e^2}{m_{\gamma'}^2} \right) \sqrt{1 - \frac{4m_e^2}{m_{\gamma'}^2}}, \quad (3.5)$$

where ζ is the Riemann Zeta function. Equation (3.5) offers a very useful estimate of the yield of heavy dark photons in the freeze-in regime. It should be interpreted as the ratio of $n_{\gamma'}$ to n_{γ} when the production has effectively ceased while the decay has not started yet. In the freeze-in regime, such a period always exists. The value of g_H should be evaluated at $T \sim m_{\gamma'}$, assuming that g_{\star} does not vary rapidly when T approaches $m_{\gamma'}$.

The validity of Eq. (3.5) only requires that $m_{\gamma'}$ is above $2m_e$ and ε is sufficiently small. It remains valid even after including the medium effect which is responsible for the resonant production—see discussions in the next section and Fig. 4.

Neglecting the factor $\left(1 + 2m_e^2/m_{\gamma'}^2 \right) \sqrt{1 - 4m_e^2/m_{\gamma'}^2}$, which only deviates from 1 by less than 10% for $m_{\gamma'} > 3m_e$, Eq. (3.5) implies

$$\frac{n_{\gamma'}}{n_{\gamma}} \approx 0.011 \times \frac{g_{\gamma'}}{g_{\gamma}} \cdot \left(\frac{\varepsilon}{10^{-10}} \right)^2 \cdot \frac{10 \text{ MeV}}{m_{\gamma'}} \cdot \left(\frac{10.75}{g_{\star}} \right)^{1/2}. \quad (3.6)$$

The freeze-in estimate would lose its validity when $n_{\gamma'}$ approaches n_{γ} . Hence for the above expression to be valid, ε should satisfy $\varepsilon \lesssim 10^{-9} \sqrt{m_{\gamma'}/10 \text{ MeV}}$.

4 The medium effect

In the thermal environment of the early universe, the photon receives a thermal correction to its self-energy from coherent scattering with the medium particles. This thermal correction, also known as the thermal mass of the photon, modifies the derivation of Eq. (2.2), which is

derived from the diagonalization of the kinetic and mass terms of gauge bosons. Note that γ and γ' are defined as mass eigenstates with canonically-normalized kinetic terms. Therefore, in the medium when the photon attains the thermal mass, these mass eigenstates, together with the derivation of Eq. (2.2), are altered by the medium effect.

The medium effect is small when $m_{\gamma'}$ is large compared to the thermal effective mass of γ . However, when $m_{\gamma'}$ is small or the medium becomes sufficiently dense and hot, the influence of the medium effect rises. In particular, if $m_{\gamma'} \rightarrow 0$, the dark photon in the medium would behave as if it is fully decoupled from the SM sector. This is the reason why most cosmological and astrophysical bounds on the dark photon vanish in the limit of $m_{\gamma'} \rightarrow 0$ [8, 40].

4.1 Basic formulism

The medium effect can be included by employing the effective in-medium mixing ε_m , which is related to the in-vacuum mixing ε as [35, 41–43]

$$\varepsilon_m = \frac{m_{\gamma'}^2}{m_{\gamma'}^2 - \Pi_{\gamma\gamma}} \varepsilon, \quad (4.1)$$

where $\Pi_{\gamma\gamma}$ denotes the photon self-energy in the thermal environment. Eq. (4.1) can be derived in various approaches—see, e.g., Eq. (15) of Ref. [41] for a derivation from the classical equation of motion, or Fig. 1 and Eq. (3.7) of Ref. [35] for a diagrammatic derivation.

Including the medium effect, the production rate of γ' in the thermal bath is given by

$$\Gamma_{\gamma'}^{\text{gain}} = \frac{m_{\gamma'}^4}{\left(m_{\gamma'}^2 - \text{Re}\Pi_{\gamma\gamma}\right)^2 + (\text{Im}\Pi_{\gamma\gamma})^2} \Gamma_{\gamma',\text{vac}}^{\text{gain}}, \quad (4.2)$$

where $\text{Re}\Pi_{\gamma\gamma}$ and $\text{Im}\Pi_{\gamma\gamma}$ are the real and imaginary parts of $\Pi_{\gamma\gamma}$, and $\Gamma_{\gamma',\text{vac}}^{\text{gain}}$ is the production rate of γ' without including the medium effect. Diagrammatically, $\Gamma_{\gamma'}^{\text{gain}}$ and $\Gamma_{\gamma',\text{vac}}^{\text{gain}}$ correspond to the Feynman diagrams in Fig. 1 with the hatched blobs equal to $\varepsilon_m e$ and εe , respectively.

The real part $\text{Re}\Pi_{\gamma\gamma}$ in certain limits has simple analytical results but in general involves an integral that requires numerical integration [44]. It is noteworthy that the integral becomes sensitive to the electron asymmetry at low temperatures below around 20 keV. In Appendix C, we briefly review the calculation of $\text{Re}\Pi_{\gamma\gamma}$ based on Ref. [44].

The imaginary part $\text{Im}\Pi_{\gamma\gamma}$ is related to the photon interaction rate Γ_γ by [45]

$$\text{Im}\Pi_{\gamma\gamma} = -\omega\Gamma_\gamma, \quad (4.3)$$

with

$$\Gamma_\gamma \equiv \Gamma_\gamma^{\text{loss}} - \Gamma_\gamma^{\text{gain}}. \quad (4.4)$$

Here $\Gamma_\gamma^{\text{gain}}$ and $\Gamma_\gamma^{\text{loss}}$ are defined as the gain and loss rates of γ in a way similar to $\Gamma_{\gamma'}^{\text{gain}}$ and $\Gamma_{\gamma'}^{\text{loss}}$ defined in Eq. (2.3). Similar to Eq. (2.3), one could also write down the Boltzmann

equation for f_γ . However, since γ is in thermal equilibrium, the right-hand side of this equation should vanish, i.e.,

$$\Gamma_\gamma^{\text{gain}}(1 + f_\gamma) - \Gamma_\gamma^{\text{loss}}f_\gamma = 0, \quad (4.5)$$

where $f_\gamma = 1/(e^{\omega/T} - 1)$ is Bose-Einstein distribution of photons in thermal equilibrium. Viewing Eqs. (4.4) and (4.5) as linear equations in $\Gamma_\gamma^{\text{gain}}$ and $\Gamma_\gamma^{\text{loss}}$, one can solve them to obtain

$$\Gamma_\gamma^{\text{gain}} = f_\gamma \Gamma_\gamma, \quad \Gamma_\gamma^{\text{loss}} = (1 + f_\gamma) \Gamma_\gamma. \quad (4.6)$$

Eq. (4.6) allows us to determine Γ_γ from $\Gamma_\gamma^{\text{gain}}$. The latter is determined by Feynman diagrams similar to those in Fig. 1. So the results can be obtained by adapting those in Tab. 1 with $\varepsilon \rightarrow 1$ and $m_{\gamma'}^2 \rightarrow \omega^2 - k^2$. Although this includes the contribution of $e^+e^- \rightarrow \gamma$, it does not imply that γ can be physically produced via this process, as the on-shell production of such photons would require $\omega^2 - k^2 > 4m_e^2$, which is kinematically forbidden for photons¹. The on-shell production of γ' via e^+e^- coalescence, however, is possible when $m_{\gamma'}^2 > 4m_e^2$ and becomes the dominant channel in the high-mass regime. When the production of γ' is significantly affected by the contribution of $e^+e^- \rightarrow \gamma$ to $\Gamma_\gamma^{\text{gain}}$ (This occurs at $T \rightarrow \frac{3}{2\sqrt{\pi\alpha}}m_{\gamma'} \approx 9.9m_{\gamma'}$ for γ' heavier than $2m_e$), it can be physically interpreted as that e^+e^- coalescence first produces an off-shell γ which is then converted, via kinetic mixing, to an on-shell γ' with the same ω and k .

Using Eq. (4.2) with $\text{Re}\Pi_{\gamma\gamma}$ and $\text{Im}\Pi_{\gamma\gamma}$ evaluated as described above, it is straightforward to calculate $\Gamma_{\gamma'}^{\text{gain}}$, at least numerically. Nevertheless, in the next two subsections, we would like to discuss some analytical features which, while not essential for the numerical evaluation, provide important insight into the thermal production of dark photons.

4.2 Resonant production

When $\text{Re}\Pi_{\gamma\gamma}$ in Eq. (4.2) approaches $m_{\gamma'}^2$, the denominator reduces to $(\text{Im}\Pi_{\gamma\gamma})^2$, indicating that the production of γ' is greatly enhanced, i.e., it enters the resonant production regime. When $\text{Im}\Pi_{\gamma\gamma}$ is small, the resonant production can be approximated by the Dirac delta function:

$$\Gamma_{\gamma'}^{\text{gain}} \approx f_\gamma \Gamma_\gamma \frac{\varepsilon^2 m_{\gamma'}^4}{(m_{\gamma'}^2 - \text{Re}\Pi_{\gamma\gamma})^2 + \omega^2 \Gamma_\gamma^2} \xrightarrow{\text{res.}} f_\gamma \varepsilon^2 m_{\gamma'}^4 \frac{\pi}{\omega} \delta(m_{\gamma'}^2 - \text{Re}\Pi_{\gamma\gamma}), \quad (4.7)$$

where we have used the identity $\lim_{y \rightarrow 0} \frac{y}{x^2 + y^2} = \pi \delta(x)$. The abbreviation “res.” above the arrows indicates that this is an approximation made near the resonance. Note that the result after taking the δ function limit becomes independent of Γ_γ . As a consequence, if we integrate the production rate around the resonance, the resulting yield of dark photons is insensitive to Γ_γ .

Substituting Eq. (4.7) into Eq. (2.5), we obtain

$$f_{\gamma'}(a, p) \approx \frac{\pi \varepsilon^2 m_{\gamma'}^4}{apH_\star} \left| \frac{d\text{Re}\Pi_{\gamma\gamma}}{da} \right|_\star^{-1} \exp\left(-\frac{ap}{a_\star T_\star}\right), \quad (4.8)$$

¹Even at high temperatures when the thermal mass of γ exceeds $2m_e$, this production channel remains kinematically forbidden because the dispersion relation of the electron is also modified [44].

where we have used the Boltzmann approximation and the relativistic approximation. Here the subscript “ \star ” indicates that the quantity should be evaluated at the resonance. Integrating over the phase space, we obtain

$$n_{\gamma'} \approx \frac{\varepsilon^2 g_{\gamma'} m_{\gamma'}^4 a_\star^2 T_\star^2}{2\pi a^3 H_\star} \left| \frac{d\text{Re}\Pi_{\gamma\gamma}}{da} \right|_\star^{-1}. \quad (4.9)$$

Using a semi-analytic expression for $\text{Re}\Pi_{\gamma\gamma}$ in Appendix C, we can further write Eq. (4.9) as

$$n_{\gamma'} \approx \left(\frac{a_\star}{a} \right)^3 \cdot \frac{9\varepsilon^2 g_{\gamma'} m_{\gamma'}^4}{16\pi^2 \alpha H_\star} F_1 \left(\frac{T_\star}{\text{MeV}} \right), \quad (4.10)$$

where

$$F_1(x) \approx \frac{1}{\frac{3}{2} x c_5^2 + \left(\frac{2}{15} x^{-\frac{6}{5}} + 1 \right) e^{-\frac{2}{9x^{6/5}}}}, \quad (4.11)$$

and $c_5 \approx 5.0 \times 10^{-5}$ is a constant determined by the electron asymmetry. Note that $F_1(x) \approx 1$ for large x .

Comparing $n_{\gamma'}$ to the photon number density n_γ , we find

$$\frac{n_{\gamma'}}{n_\gamma} \approx \frac{9\varepsilon^2 g_{\gamma'} m_{\gamma'}^4 m_{\text{pl}}}{16\zeta(3)\alpha g_\gamma g_H T_\star^5} F_1 \left(\frac{T_\star}{\text{MeV}} \right). \quad (4.12)$$

This result should be understood as the value of $n_{\gamma'}/n_\gamma$ shortly after the resonant production. Subsequent evolution could modify it via, e.g., dark photon decay or entropy dilution.

If the resonance occurs when electrons are still relativistic ($T_\star \gtrsim m_e$), Eq. (4.12) reduces to

$$\frac{n_{\gamma'}}{n_\gamma} \approx 0.015 \times \left(\frac{\varepsilon}{10^{-10}} \right)^2 \cdot \frac{1 \text{ MeV}}{m_{\gamma'}} \cdot \left(\frac{10.75}{g_\star} \right)^{1/2}, \quad (4.13)$$

which is a simple and convenient formula for estimating the freeze-in yield of resonant production. In practice, we find that Eq. (4.13) is valid for $m_{\gamma'} \gtrsim 0.05 \text{ MeV}$. For lower masses, we recommend using Eq. (4.12) with Eq. (4.11) to estimate the ratio.

After the resonance, the production of γ' proceeds at a rate without significant enhancement from the medium effect (In particular, when $\text{Re}\Pi_{\gamma\gamma} \ll m_{\gamma'}^2$, the rate is well approximated by $\Gamma_{\gamma',\text{vac}}^{\text{gain}}$). However, this does not necessarily mean that the resonant production makes the dominant contribution throughout the entire evolution. In the high-mass regime with $m_{\gamma'} > 2m_e$, the resonance occurs at $T \approx 9.9m_{\gamma'}$ but at $T \sim m_{\gamma'}$ the inverse decay process also contributes significantly, as we have estimated in Sec. 3.3. It is therefore interesting to compare Eq. (4.13) or (4.12) with Eq. (3.6) or (3.5). Note that Eq. (4.12) is proportional to $\alpha^{3/2}$ because $T_\star \propto \alpha^{-1/2}$ and $F_1 \approx 1$, while Eq. (3.5) is proportional to α . Hence we expect that the resonant production is subdominant in the high-mass regime. Indeed, if we compute the ratio of Eq. (4.12) to (3.5), we find

$$\boxed{\frac{(n_{\gamma'} a^3)_{\text{res.}}}{(n_{\gamma'} a^3)_{\text{ID}}} \approx \frac{4\pi e}{27} + \mathcal{O} \left(\frac{m_e^4}{m_{\gamma'}^4} \right) \approx 0.14.} \quad (4.14)$$

Here the subscript “res.” and “ID” indicate the contributions from the resonant production and from the post-resonance inverse decay process. In Sec. 5, we will show that Eq. (4.14) agrees very well with numerical solutions—see Fig. 4.

4.3 Photon-dark photon oscillation

Although the photon and dark photon are in a diagonal basis after their kinetic terms are canonically diagonalized in vacuum [i.e., the step from Eq. (2.1) to Eq. (2.2)], the medium effect reintroduces an effective mixing between them. Consequently, when photons propagate from vacuum to medium, or through medium with varying density, photon-dark photon oscillation can occur. This is analogous to neutrino oscillations affected by the matter effect [46–48], or to photon-axion conversion (or oscillation) in magnetic fields—see, e.g., [49].

The oscillation length of $\gamma \leftrightarrow \gamma'$ is of the order $\omega/\Delta m^2$ where Δm^2 denotes the mass squared difference between the two particles. This length is to be compared with the mean free path of γ , given by $1/\Gamma_\gamma^{\text{loss}} \sim 1/\Gamma_\gamma$. If the oscillation length is larger than $1/\Gamma_\gamma$, the photon is likely to be absorbed by the medium before it oscillates to γ' . By requiring $\omega/\Delta m^2 \ll 1/\Gamma_\gamma$, corresponding to $\Gamma_\gamma \omega \ll \Delta m^2$, one can use photon-dark photon oscillation to compute the production of γ' . A full treatment of photon-dark photon oscillation in the expanding universe, where the medium varies with time (one can also regard it as variation along the propagation path), is rather involved and not necessary here, since within its validity range it is equivalent to the calculation presented above. Below we demonstrate some illuminating features in the oscillation framework that may deepen our understanding of the dark-photon production in thermal medium.

Let us consider a simple scenario in which a photon propagates from vacuum, through a slab of medium, and then back into vacuum, as illustrated in Fig. 3. In vacuum, the photon can never be converted to a dark photon since the kinetic mixing has been eliminated when canonically diagonalizing the kinetic terms. In the slab of medium, there is a small probability that this conversion can happen, since the medium generates an effective operator,² $\mathcal{L} \supset \Pi_{\gamma\gamma'} A^\mu A'_\mu$ where $\Pi_{\gamma\gamma'} = \varepsilon \Pi_{\gamma\gamma}$. Then the following matrix element gives rise to the conversion amplitude:

$$\langle \mathbf{k}_2 | \overbrace{\Pi_{\gamma\gamma'} A^\mu A'_\mu}^{\text{medium}} | \mathbf{k}_1 \rangle \rightarrow \mathcal{A}_{\gamma \rightarrow \gamma'}. \quad (4.15)$$

Here $|\mathbf{k}_1\rangle$ and $|\mathbf{k}_2\rangle$ denote the initial and final states of γ and γ' , respectively. Note that, as indicated in Fig. 3, they share the same energy ω but their momenta are different, which implies that there is a small momentum transfer to/from the medium, a well-known aspect in photon refraction.

After performing the Wick contraction, we obtain³

$$\mathcal{A}_{\gamma \rightarrow \gamma'} = \frac{1}{2\sqrt{|\mathbf{k}_1||\mathbf{k}_2|}} \int dx \Pi_{\gamma\gamma'}(x) e^{i|\mathbf{k}_1 - \mathbf{k}_2|x}. \quad (4.16)$$

²See e.g. Appendix B in [35] for an explicit calculation of the coherent scattering with medium particles that generates the operator.

³See Eq. (A.21) in [49] for a derivation.

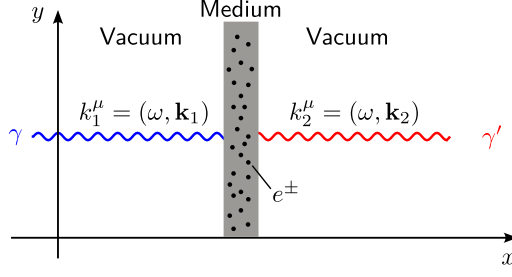


Figure 3. Schematic illustration of the slab approximation used to derive γ - γ' oscillation.

The integral in Eq. (4.16) is essentially a Fourier transform of $\Pi_{\gamma\gamma'}(x)$ which we assume is a constant in the slab, i.e.,

$$\Pi_{\gamma\gamma'}(x) = \begin{cases} \Pi_{\gamma\gamma'} & x \in [0, L] \\ 0 & \text{otherwise} \end{cases}. \quad (4.17)$$

Substituting Eq. (4.17) into Eq. (4.16), we get

$$\mathcal{A}_{\gamma \rightarrow \gamma'} = \frac{\Pi_{\gamma\gamma'}}{2\sqrt{|\mathbf{k}_1||\mathbf{k}_2|}} \left(\frac{e^{i|\mathbf{k}_1 - \mathbf{k}_2|L} - 1}{|\mathbf{k}_1 - \mathbf{k}_2|} \right). \quad (4.18)$$

So the probability of the conversion reads

$$P_{\gamma \rightarrow \gamma'} = |\mathcal{A}_{\gamma \rightarrow \gamma'}|^2 \approx 4\varepsilon^2 \left| \frac{\Pi_{\gamma\gamma}}{m_{\gamma'}^2 - m_\gamma^2} \right|^2 \sin^2 \left(\frac{m_{\gamma'}^2 - m_\gamma^2}{4\omega} L \right), \quad (4.19)$$

where we have used the relativistic approximation for both γ and γ' . A hypothetical mass of the photon, m_γ , is introduced for later convenience. Eq. (4.19) implies that the conversion probability indeed oscillates with L . In the slab approximation one might think that L has to be short, but actually it is microscopically long compared to the wavelength $\sim \omega/\Delta m^2$. In addition, as long as the medium is constant, static, and transparent to γ/γ' , the above calculation is always valid for arbitrarily long L .

One can also use Eq. (4.19) to obtain the resonant production rate discussed in Sec. 4.2. Using

$$\delta(x) = \frac{1}{\pi} \lim_{y \rightarrow \infty} \frac{\sin^2(xy)}{x^2 y}, \quad (4.20)$$

we see that in the large L limit, Eq. (4.19) reduces to

$$P_{\gamma \rightarrow \gamma'} \rightarrow \varepsilon^2 |\Pi_{\gamma\gamma}|^2 \pi \frac{L}{\omega} \delta(m_{\gamma'}^2 - m_\gamma^2). \quad (4.21)$$

Dividing it by L (so that it can be interpreted as the differential conversion probability per unit length) and multiplying it by f_γ (which is related to the number of photons), we arrive at

$$f_\gamma \frac{P_{\gamma \rightarrow \gamma'}}{L} \rightarrow \varepsilon^2 m_\gamma^4 \pi \frac{\pi}{\omega} \delta(m_{\gamma'}^2 - m_\gamma^2), \quad (4.22)$$

which is essentially the same as the resonant production rate in Eq. (4.7).

5 Evolution

The cosmological evolution of dark photons can be obtained by solving the Boltzmann equation. In this section, we numerically solve the Boltzmann equation for $n_{\gamma'}$ with the collision terms in Tab. 1. The medium effect is included using Eq. (4.2).

In the lower panels of Fig. 4, we show the solutions of two benchmarks with $m_{\gamma'} \in \{3, 0.5\}$ MeV and $\varepsilon = 10^{-11}$. As previously discussed, when the temperature reaches a certain value, the resonant production is achieved. Indeed, one can see that within the orange bands shown in Fig. 4, $n_{\gamma'}/s$ increases rapidly. On the upper panels, we present the corresponding $C_{\gamma'}^{\text{gain}}-T$ curves, which exhibit sharp peaks at $T \approx 30$ and 5 MeV.

After the resonance, the evolution may or may not be able to produce a significant extra amount of dark photons, depending on whether the inverse decay process is kinematically allowed or not. For the benchmark with $m_{\gamma'} = 3$ MeV, which is above $2m_e$, the inverse decay process becomes effective during the period indicated by the green band in Fig. 4. In this case, the post-resonance evolution generates more dark photons through inverse decay than the resonance. Hence the $n_{\gamma'}/s$ curve exhibits two plateaus, one occurring after the resonance (after T reaches about 30 MeV) and the other occurring after the completion of inverse decay. Both can be analytically estimated, as given by Eqs. (4.13) and (3.6). The second plateau is expected to be a factor of $4\pi e/27 \approx 0.14$ higher than the first, according to Eq. (4.14). Since this benchmark is in the freeze-in regime, the dark photon is relatively long-lived compared to the cosmic time $t \approx 1/(2H)$. After reaching the second plateau, the number of dark photons in a comoving volume remains approximately constant until t becomes comparable to its lifetime $\tau_{\gamma'}$. At $t \gtrsim \tau_{\gamma'}$, corresponding to the gray band in Fig. 4, the number decreases exponentially.

By contrast, the evolution of the benchmark with $m_{\gamma'} = 0.5$ MeV (right panels in Fig. 4) has a simpler structure: the $n_{\gamma'}/s$ curve increases rapidly during resonant production and reaches a stable value that can be estimated by Eq. (4.13). The post-resonance production makes only a negligible contribution. Since the two-body decay channel $\gamma' \rightarrow e^+e^-$ is forbidden for $m_{\gamma'} < 2m_e$, the dark photon in this example is extremely long-lived, with $\tau_{\gamma'}$ comparable to the age of universe $\tau_U \approx 4.35 \times 10^{17}$ sec. Consequently, the $n_{\gamma'}/s$ curve remains essentially flat throughout the cosmic history from the resonant production to the present epoch. The abundance of these long-lived dark photons could be slightly reduced by $\gamma' + e^- \rightarrow \gamma + e^-$, but this effect is negligibly small for this benchmark. More generally, we find that as long as ε lies in the freeze-in regime, this process never becomes significant in the evolution of dark photons.

Here we would like to comment on possible decay channels of γ' in the low-mass regime ($m_{\gamma'} < 2m_e$). In this regime, without introducing extra light species, γ' can only decay to species lighter than electrons, namely photons and neutrinos (ν). Decaying to two photons ($\gamma' \rightarrow 2\gamma$) is not allowed as this would violate the Landau–Yang theorem. Decaying to three photons ($\gamma' \rightarrow 3\gamma$, arising from a loop diagram) is allowed, with the following decay width [50]

$$\Gamma_{\gamma' \rightarrow 3\gamma} \approx \frac{17\varepsilon^2\alpha^4}{11664000\pi^3} \frac{m_{\gamma'}^9}{m_e^8}. \quad (5.1)$$

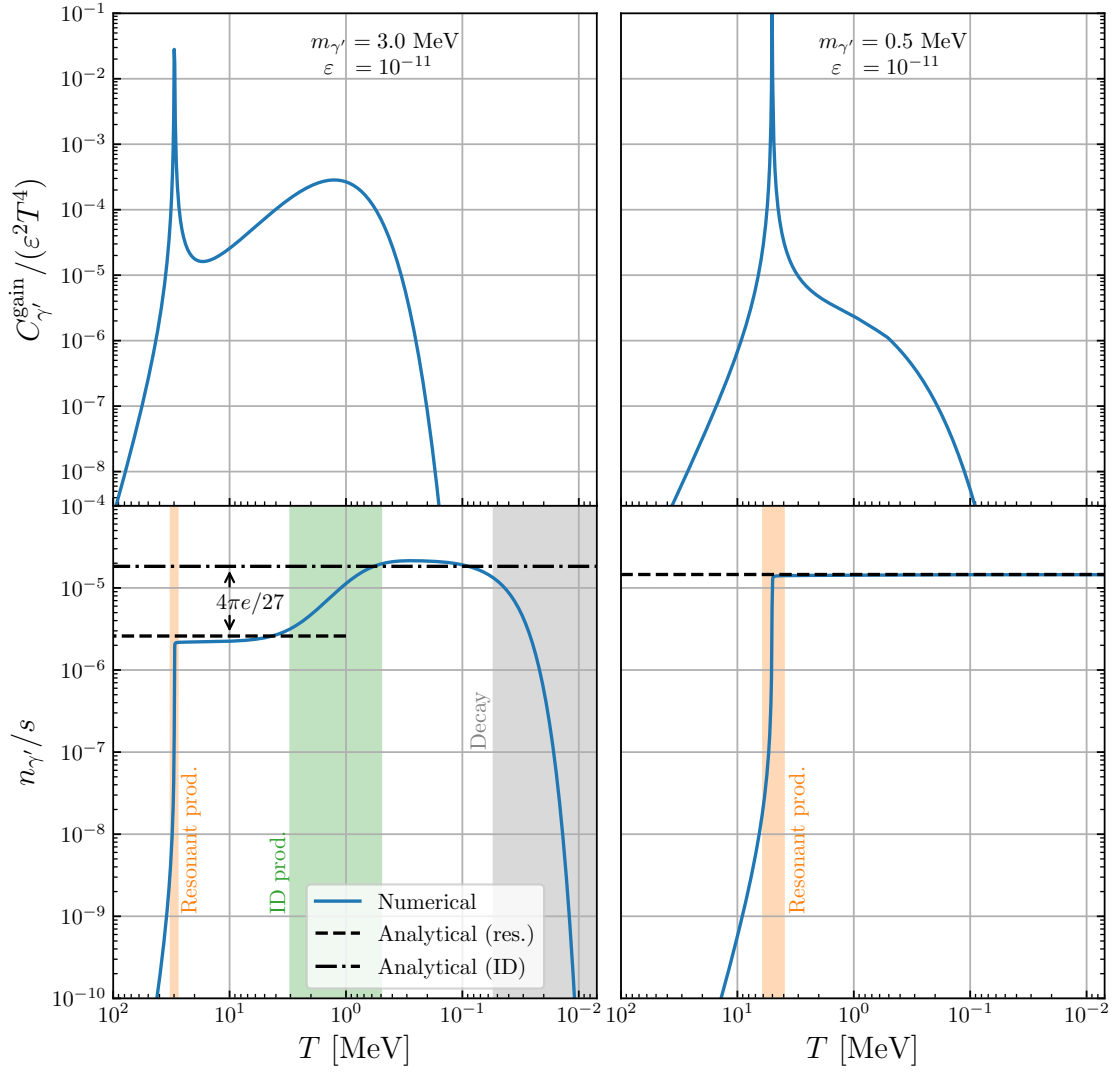


Figure 4. Upper panels: Resonances of the production rate; Lower panels: the evolution of the dark photon number density $n_{\gamma'}$ divided by the entropy density s . The dashed and dash-dotted lines represent our analytical estimates given by Eqs. (4.13) and (3.6). The gap between them, $4\pi e/27 \approx 0.14$, is estimated by Eq. (4.14).

Note that Eq. (5.1) is derived in the Euler-Heisenberg limit, which implies that it may be not very accurate when $m_{\gamma'}$ approaches $2m_e$ —see Refs. [51–53] for discussions on small deviations from this limit. Since a precise calculation of $\Gamma_{\gamma' \rightarrow 3\gamma}$ is not required in this work, Eq. (5.1) suffices for our analysis. Regarding the possibility of decaying to neutrinos ($\gamma' \rightarrow 2\nu$), this is implied by Eq. (2.1) where $F^{\mu\nu}$ contains a small component of the Z boson. However, the resulting coupling of γ' to neutrinos is suppressed by $s_W m_{\gamma'}^2 / m_Z^2$ [34, 35]. We have estimated the decay width of $\gamma' \rightarrow 2\nu$ and find that it is sufficiently small to be neglected in this work.

In the left panel of Fig. 5, we scan over a wide range of $m_{\gamma'}$ covering both the high-

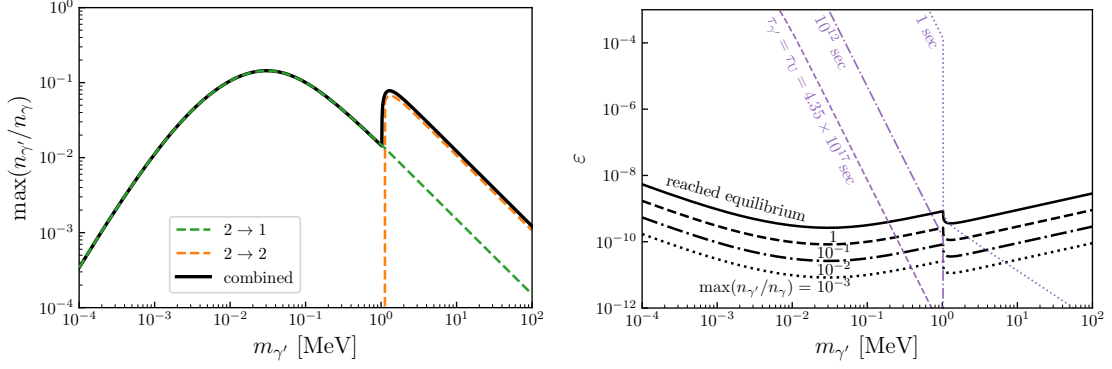


Figure 5. Left: The maximum of $n_{\gamma'}/s$ during the evolution as a function of $m_{\gamma'}$, assuming $\varepsilon = 10^{-10}$. Right: Contours on the ε - $m_{\gamma'}$ plane to indicate whether γ' has ever reached equilibrium (black lines) and whether it is long-lived (purple lines).

mass and low-mass regimes with $\varepsilon = 10^{-10}$ and plot $\max(n_{\gamma'}/n_{\gamma})$ as a function of $m_{\gamma'}$. Here “max” takes the maximum of $n_{\gamma'}/n_{\gamma}$ during the evolution. This maximum is used to quantify how close the evolution is to thermal equilibrium. In this plot, the curves labeled $2 \rightarrow 1$ and $2 \rightarrow 2$ represent contributions from inverse decay and from scattering processes (semi-Compton and annihilation), while the black curve includes both. As shown in this plot, the black curve is always significantly below 1, implying that dark photons with $\varepsilon = 10^{-10}$ can never reach thermal equilibrium.

In the right panel of Fig. 5, we show the contours of $\max(n_{\gamma'}/n_{\gamma}) = 10^{-3}, 10^{-2}, 10^{-1}$ and 1 on the ε - $m_{\gamma'}$ plane. In the region above the black solid line, dark photons have reached thermal equilibrium. In this plot, we also show the lifetime contours (purple lines) corresponding to $\tau_{\gamma'} = 4.35 \times 10^{17}$ sec (the age of the Universe), 10^{12} sec (the time scale at $T = 1$ eV), and 1 sec (the time scale at $T = 1$ MeV). For $\tau_{\gamma'} \lesssim 1$ sec, dark photons decay after neutron freeze-out and neutrino decoupling. For $\tau_{\gamma'} \ll 10^{12}$ sec, dark photons within the shown mass range are non-relativistic long-lived particles at recombination (0.3 eV) and the matter-radiation equality (0.8 eV), implying that they play a role of dark matter at this epoch. Note that within the gap between the dash-dotted ($\tau_{\gamma'} = 10^{12}$ sec) and dashed ($\tau_{\gamma'} = \tau_U$) purple lines, dark photons would behave as dark matter for CMB observations but cannot contribute to the present-day dark matter.

6 Cosmological constraints

Dark photons being thermally produced in the early Universe are subjected to various cosmological constraints from BBN and CMB measurements. For instance, the energy carried by dark photons may contribute significantly to the Hubble expansion rate, which influences out-of-equilibrium processes including neutrino decoupling and neutron freeze-out. Both are important to BBN predictions. If dark photons carry a significant amount of energy at neutrino decoupling and then subsequently decay into electromagnetic radiation, assuming the lifetime $\tau_{\gamma'} \in [10^{-12}, 1]$ sec, the neutrino-to-photon temperature ratio

$T_\nu/T_\gamma \approx (4/11)^{1/3}$ in the standard cosmology is reduced. Consequently, the effective number of neutrino species (N_{eff}) in CMB measurements receives a negative contribution. Note that N_{eff} is also an important observable in BBN, but for BBN, dark photons in the freeze-in regime behave as dark radiation during neutron freeze-out. Consequently, the N_{eff} measured by BBN receives a positive contribution. To distinguish between the two observables, we refer to them as $N_{\text{eff}}^{\text{BBN}}$ and $N_{\text{eff}}^{\text{CMB}}$ when they are measured by BBN and CMB, respectively. The latest measurements of $N_{\text{eff}}^{\text{BBN}}$ and $N_{\text{eff}}^{\text{CMB}}$ are $N_{\text{eff}}^{\text{BBN}} = 2.898 \pm 0.141$ [54] and $N_{\text{eff}}^{\text{CMB}} = 2.99 \pm 0.17$ [55]. Therefore, the positive contribution to $N_{\text{eff}}^{\text{BBN}}$, denoted $\Delta N_{\text{eff}}^{\text{BBN}}$, is constrained to be $\Delta N_{\text{eff}}^{\text{BBN}} \lesssim 0.3$ at 3σ C.L., while the negative contribution is constrained to be $\Delta N_{\text{eff}}^{\text{CMB}} \gtrsim -0.6$ also at 3σ C.L.

In the left panel of Fig. 6, the red region is excluded by $\Delta N_{\text{eff}}^{\text{BBN}} > 0.3$ where $\Delta N_{\text{eff}}^{\text{BBN}}$ is computed by $\Delta N_{\text{eff}}^{\text{BBN}} = \rho_{\gamma'}/\rho_\nu$ at $T = 1$ MeV, which is approximately the temperature of neutron freeze-out. The red dashed and dotted contours correspond to $\Delta N_{\text{eff}}^{\text{BBN}} = 0.2$ and 0.1 . These $\Delta N_{\text{eff}}^{\text{BBN}}$ contours exhibit a few noteworthy features. Their right edges are nearly vertical, except for a small “nose” in the lower-right corner. The vertical part arises from that the energy density of thermalized (i.e., in equilibrium) dark photons is independent of ε . The value of $\rho_{\gamma'}$ at $T = 1$ MeV is Boltzmann suppressed for heavy dark photons with $m_{\gamma'} \gg 1$ MeV. So when $m_{\gamma'}$ exceeds certain values (about 6 MeV), the resulting $\Delta N_{\text{eff}}^{\text{BBN}}$ becomes negligibly small. The “nose” is a consequence of the interplay between the Boltzmann suppression and freeze-in, occurring when the system is near the boundary of thermal equilibrium—see Fig. 2 in Ref. [56] for illustration. The left edges of these contours are also very steep. This part corresponds to the scenario that the resonant production occurs at sub-MeV or even lower temperatures. At temperatures above the MeV scale, dark photons in this regime have $m_{\gamma'}^2 \ll \text{Re}\Pi_{\gamma\gamma}$. As a consequence, the production rate is suppressed by $m_{\gamma'}^4/(\text{Re}\Pi_{\gamma\gamma})^2$ according to Eq. (4.2) and becomes very sensitive to $m_{\gamma'}$.

For dark photons with $m_{\gamma'} < 2m_e$, their contribution to the total energy budget in the recombination epoch ($t \sim 10^{12}$ sec) provides a more restrictive constraint than $\Delta N_{\text{eff}}^{\text{BBN}}$. According to the right panel of Fig. 5, a very large part of the parameter space in this regime generates long-lived ($\gtrsim 10^{12}$ sec) dark photons, which become non-relativistic in the recombination epoch. Hence dark photons in this regime contribute to the dark matter in the recombination epoch. The energy density of dark matter in this epoch is given by $\rho_{\text{DM}} \approx 9.74 \times 10^{-12} \text{ eV}^4 \times (T/T_0)^3$ with $T_0 \approx 2.73$ K the present CMB temperature. By requiring $\rho_{\gamma'}/\rho_{\text{DM}} < 1$ at $T = 1$ eV, we obtain the constraint of dark matter overproduction, represented by the purple region in the left panel of Fig. 6.

The cosmological constraints discussed above are based solely on energy-density considerations. They are rather robust even in the presence of extra new physics such as interacting with dark-sector particles. For instance, if γ' possesses dark decay channels, the $\Delta N_{\text{eff}}^{\text{BBN}}$ bound would be largely unaffected or even become stronger than the one shown here. The dark matter overproduction bound may be altered but combining the requirements of not overproducing dark matter, dark radiation, and other components during the recombination epoch would lead to a similar bound. In addition to the constraints based on energy-density considerations, one can also derive constraints that rely on electromagnetic

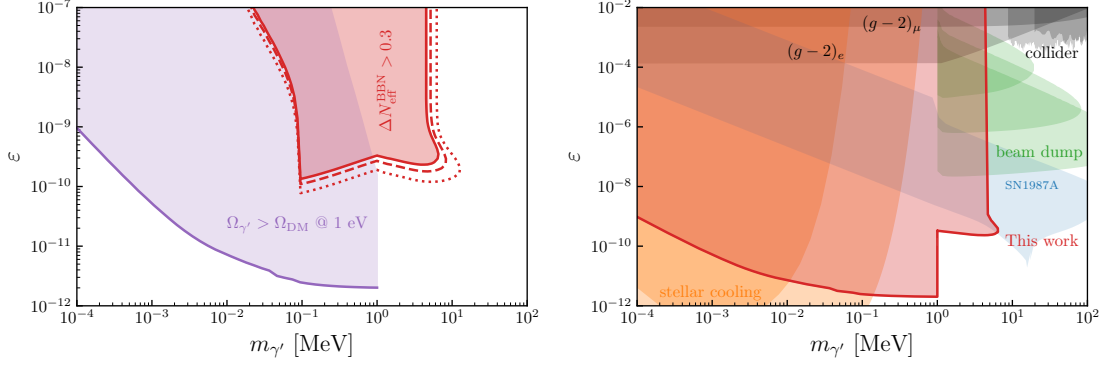


Figure 6. Cosmological bounds on the dark photon derived in this work (left panel) and compared with other known bounds (right panel). The two shaded regions on the left panel are excluded by $\Omega_{\gamma'} > \Omega_{\text{DM}}$ at $T = 1$ eV and by $\Delta N_{\text{eff}}^{\text{BBN}} > 0.3$. The red dashed and dotted contours correspond to $\Delta N_{\text{eff}}^{\text{BBN}} = 0.2$ and 0.1 , respectively. On the right panel, we combine the two cosmological bounds and present it as the red shaded region. For other known bounds, see the main text for more details.

radiation generated by dark photons. For BBN, energetic photons arising from dark photon decay may cause photo-dissociation of light elements [23, 57–59]. For CMB, electromagnetic radiation injected into the background photons may cause significant CMB spectral distortions [60, 61] and anisotropy signals [62]. We leave dedicated analyses of these effects to future work.

In the right panel of Fig. 6, we combine the two cosmological bounds based on energy-density considerations together and compare it with other known bounds. Here, the orange regions are excluded by stellar cooling, taken from Ref. [35]. The blue region represent the bound derived from supernovae, taken from Ref. [63]. The laboratory bounds derived from $(g-2)_\mu$, $(g-2)_e$, collider, and beam dump experiments are generated using the **DARCAST** package [5]. In comparison with these bounds, the cosmological bound is most stringent in the mass range from 0.1 MeV to 6 MeV.

7 Conclusion

In this work, we comprehensively studied the thermal production of dark photons in the early universe. Three processes responsible for the thermal production (inverse decay, annihilation, and semi-Compton) were calculated both analytically and numerically. The analytical expressions for the collision terms of these processes are summarized in Tab. 1 and exhibit excellent accuracy within their valid ranges, as shown in Fig. 2.

The analytical collision terms allow us to perform various subsequent calculations analytically. Among them, we would like to highlight the ratio, $(n_{\gamma'} a^3)_{\text{res.}} / (n_{\gamma'} a^3)_{\text{ID}} \approx 4\pi e / 27 \approx 0.14$, where $(n_{\gamma'} a^3)_{\text{res.}}$ and $(n_{\gamma'} a^3)_{\text{ID}}$ denote the numbers of dark photons in a comoving volume produced through the resonance and off-resonance inverse decay, respectively. This ratio is broadly valid and insensitive to the dark photon mass $m_{\gamma'}$ and the kinetic mixing ε , provided that ε is in the freeze-in regime and $m_{\gamma'} > 2m_e$. For dark

photons with $m_{\gamma'} < 2m_e$, we find that the off-resonance production is negligible and the yield can be simply estimated using the resonant production. For both light and heavy dark photons, our analytical estimates are in good agreement with numerical solutions of the Boltzmann equation, as shown in Fig. 4.

Finally, we present the cosmological constraints on the dark photon derived solely from energy-density considerations: they only require that $\rho_{\gamma'}/\rho_\nu$ at 1 MeV and $\rho_{\gamma'}/\rho_{\text{DM}}$ at 1 eV do not exceed the limits allowed by BBN and CMB observations. The constraints obtained in this way are relatively conservative and robust against potential variations arising from new interactions with other dark-sector particles. Compared with known bounds from stellar cooling, supernovae, and laboratory searches, the cosmological constraints are most stringent in the mass range from 0.1 MeV to 6 MeV, within which they are capable of probing kinetic mixing at the level of 10^{-12} – 10^{-10} .

We hope that the analytical estimates and cosmological constraints presented in this work may provide useful tools for ongoing studies of dark photons and related new particles.

Note added: As we were finalizing this work, Ref. [64] appeared on arXiv. It also focuses on the dark photon within a very similar mass regime and contains the calculation of its thermal production in the early universe. While many technical details in Ref. [64] differ from ours, the main calculation procedure is similar, with the final results in good agreement with each other. Compared to Ref. [64], our work is more focused on the analytical discussions.

Acknowledgments

This work is supported in part by the National Natural Science Foundation of China under grant No. 12141501 and also by the CAS Project for Young Scientists in Basic Research (YSBR-099).

A Lorentz-invariant phase space integral

In this work, the following phase space integral is often encountered:

$$I_{34} = \int d\Pi_3 d\Pi_4 (2\pi\delta)^4 |\mathcal{M}|^2, \quad (\text{A.1})$$

where $|\mathcal{M}|^2$ is the squared matrix element of a generic 2-to-2 process, $1 + 2 \rightarrow 3 + 4$. If derived from a theory respecting Lorentz invariance, $|\mathcal{M}|^2$ should be Lorentz invariant, and its dependence on kinematics can be fully characterized by the three Mandelstam variables, $s = (p_1 + p_2)^2$, $t = (p_1 - p_3)^2$, and $u = (p_1 - p_4)^2$. Then Eq. (A.1) is fully Lorentz-invariant, implying that it can be conveniently calculated in, e.g., the center-of-mass frame, and the result remains invariant when boosted to a general frame.

By recasting the relevant formulae in Chapter 49: *Kinematics* of Ref. [54] into Lorentz-invariant forms, we obtain

$$\int d\Pi_3 d\Pi_4 (2\pi\delta)^4 |\mathcal{M}|^2 = \frac{1}{8\pi\sqrt{\lambda_{s12}}} \int_{t_-}^{t_+} |\mathcal{M}|^2 dt, \quad (\text{A.2})$$

where

$$t_{\pm} \equiv \frac{1}{2s} \left(\kappa \pm \sqrt{\lambda_{s12}\lambda_{s34}} \right), \quad (\text{A.3})$$

$$\kappa \equiv -s^2 + (m_1^2 + m_2^2 + m_3^2 + m_4^2) s - (m_1^2 - m_2^2) (m_3^2 - m_4^2), \quad (\text{A.4})$$

$$\lambda_{sij} \equiv \lambda(s, m_i^2, m_j^2), \quad (\text{A.5})$$

and $\lambda(a, b, c) \equiv a^2 + b^2 + c^2 - 2ab - 2bc - 2ca$ is the Källén function.

If $|\mathcal{M}|^2$ happens to be independent of t and u , then Eq. (A.2) reduces to

$$\int d\Pi_3 d\Pi_4 (2\pi\delta)^4 = \frac{\sqrt{\lambda_{s34}}}{8\pi s}, \quad (\text{A.6})$$

which can be used to calculate phase space integrals of 1-to-2 or 2-to-1 processes.

If one needs to integrate out the two initial momenta in $1 + 2 \rightarrow 3 + 4$ or $1 + 2 \rightarrow 3$, then the following integral can be used:

$$\int d\Pi_1 d\Pi_2 (2\pi\delta)^4 |\mathcal{M}|^2 = \begin{cases} \frac{1}{8\pi\sqrt{\lambda_{s34}}} \int_{t_-}^{t_+} |\mathcal{M}|^2 dt & (\text{for } 1 + 2 \rightarrow 3 + 4) \\ \frac{\sqrt{\lambda_{s12}}}{8\pi s} |\mathcal{M}|^2 & (\text{for } 1 + 2 \rightarrow 3) \end{cases}. \quad (\text{A.7})$$

Below, we present an example to demonstrate the use of Eqs. (A.2) and (A.6). Consider the following integral

$$I_{1234} = \int d\Pi_1 d\Pi_2 d\Pi_3 d\Pi_4 f_1 f_2 (2\pi\delta)^4 |\mathcal{M}|^2, \quad (\text{A.8})$$

where $f_{1,2} = \exp(-E_{1,2}/T)$, $m_{1,2,3,4} = 0$, and $|\mathcal{M}|^2 = (p_1 \cdot p_2)(p_3 \cdot p_4) = \frac{s^2}{4}$. This integral occurs in relativistic neutrino scattering in the early universe and its result is known: $I_{1234} = \frac{3T^8}{8\pi^5}$ [39, 65]. Since $|\mathcal{M}|^2$ is independent of t , using Eq. (A.6), we quickly obtain

$$\begin{aligned} I_{1234} &= \int d\Pi_1 d\Pi_2 f_1 f_2 \frac{s^2}{4} \frac{\sqrt{\lambda_{s34}}}{8\pi s} \\ &= \int d\Pi_1 d\Pi_2 f_1 f_2 \frac{s^2}{32\pi} \\ &= \int \frac{4\pi p_1^2 dp_1}{(2\pi)^3 2p_1} \frac{2\pi p_2^2 dp_2 dc_{12}}{(2\pi)^3 2p_2} f_1 f_2 \frac{4p_1^2 p_2^2 (1 - c_{12})^2}{32\pi} \\ &= \int \frac{4\pi p_1^2 dp_1}{(2\pi)^3 2p_1} \frac{2\pi p_2^2 dp_2}{(2\pi)^3 2p_2} e^{-(p_1 + p_2)/T} \frac{p_1^2 p_2^2}{3\pi} \\ &= \frac{3T^8}{8\pi^5}, \end{aligned} \quad (\text{A.9})$$

where $c_{12} = \cos \theta_{12}$ with θ_{12} the angle between \mathbf{p}_1 and \mathbf{p}_2 . This reproduces exactly the expected result.

B Collision terms

The collision terms for the inverse decay process can be readily obtained using Eq. (A.7), given that both $|\mathcal{M}|^2$ and $f_1 f_2 = e^{-E_1/T} e^{-E_2/T} = e^{-E_3/T}$ in Eq. (3.1) factor out of the integral. Below, we present the calculations for the annihilation and semi-Compton processes.

B.1 Annihilation

The squared amplitude of annihilation ($e^- + e^+ \rightarrow \gamma + \gamma'$), after averaging over all spins and polarizations of initial and final states, reads

$$|\mathcal{M}_A|^2 = \frac{e^4 \varepsilon^2}{3} \left(\frac{t_e}{u_e} + \frac{u_e}{t_e} \right) - \frac{2e^4 \varepsilon^2 (2 + r_{m,e})}{3} \left[\left(\frac{1}{t_e} + \frac{1}{u_e} \right) \left(\frac{1}{t_e} + \frac{1}{u_e} + 1 \right) - \frac{r_{m,e}}{t_e u_e} \right], \quad (\text{B.1})$$

where we have used the following notations:

$$r_{m,e} \equiv m_{\gamma'}^2 / m_e^2, \quad (\text{B.2})$$

$$s_e \equiv s / m_e^2, \quad (\text{B.3})$$

$$t_e \equiv t / m_e^2 - 1, \quad (\text{B.4})$$

$$u_e \equiv u / m_e^2 - 1. \quad (\text{B.5})$$

Here s, t, u are the Mandelstam variables.

The production rate of γ' through this process is given by

$$\Gamma_A^{\text{gain}} = \frac{g_1 g_2 g_3}{2\omega} \int d\Pi_1 d\Pi_2 d\Pi_3 (2\pi\delta)^4 |\mathcal{M}_A|^2 f_1 f_2, \quad (\text{B.6})$$

where $f_1 f_2 = e^{-(E_1+E_2)/T} = e^{-(E_3+\omega)/T}$ allows us to pull it out of the integral $\int d\Pi_1 d\Pi_2$.

Using Eq. (A.7), we first integrate out $d\Pi_1$ and $d\Pi_2$:

$$\begin{aligned} I_{12} &= \int d\Pi_1 d\Pi_2 (2\pi\delta)^4 |\mathcal{M}_A|^2 \\ &= \frac{\sqrt{\lambda_{s12}}}{32\pi^2 s} \int d\Omega |\mathcal{M}_A|^2 \\ &= \frac{1}{32\pi^2} \sqrt{1 - \frac{4m_e^2}{s}} \int d\Omega |\mathcal{M}_A|^2 \\ &= \frac{2(r_{m,e}^2 - 4r_{m,e} + 4s_e + s_e^2 - 8) \tanh^{-1} z_e - (r_{m,e}^2 + 4s_e + s_e^2) z_e}{12\pi(r_{m,e} - s_e)^2 / (e^4 \varepsilon^2)}, \end{aligned} \quad (\text{B.7})$$

with $z_e \equiv \sqrt{1 - 4/s_e}$.

Then Eq. (B.6) reduces to

$$\begin{aligned} \Gamma_A^{\text{gain}} &= \frac{g_1 g_2 g_3}{2\omega} e^{-\omega/T} \int d\Pi_3 e^{-E_3/T} I_{12} \\ &= \frac{g_1 g_2 g_3}{2\omega} e^{-\omega/T} \times \frac{1}{8\pi^2} \int p_3 dp_3 d\cos\theta e^{-E_3/T} I_{12}, \end{aligned} \quad (\text{B.8})$$

where θ is the angel between \mathbf{p}_4 and \mathbf{p}_3 .

Next, we change the integration variables using

$$p_3 dp_3 d\cos\theta = \frac{ds dp_3}{2p_4}, \quad (\text{B.9})$$

which can be obtained from

$$s = m_{\gamma'}^2 + 2p_3 (\omega - p_4 \cos\theta). \quad (\text{B.10})$$

Note that the kinematics of this process should always satisfy

$$s \geq 4m_e^2. \quad (\text{B.11})$$

Given fixed values of ω and s , p_3 cannot take arbitrary values, otherwise $\cos\theta$ calculated from Eq. (B.10) may reach unphysical values. From Eq. (B.10), one can derive the integration interval of p_3

$$p_3 \in \frac{1}{2} \left[\frac{s - m_{\gamma'}^2}{\omega + p_4}, \frac{s - m_{\gamma'}^2}{\omega - p_4} \right] \equiv [p_L, p_H]. \quad (\text{B.12})$$

With the integration interval determined, we can integrate out p_3 :

$$\begin{aligned} \Gamma_A^{\text{gain}} &= \frac{g_1 g_2 g_3 e^{-\omega/T}}{32\pi^2 \omega p_4} \int_{4m_e^2}^{\infty} ds \int_{p_L}^{p_H} dp_3 e^{-p_3/T} I_{12} \\ &= \frac{g_1 g_2 g_3 T e^{-\omega/T}}{32\pi^2 \omega p_4} \int_{4m_e^2}^{\infty} ds \left(e^{-p_L/T} - e^{-p_H/T} \right) I_{12}. \end{aligned} \quad (\text{B.13})$$

■ High-temperature limit:

When $T \gg m_e$, we approximate $|\mathcal{M}_A|^2$ and I_{12} as

$$|\mathcal{M}_A|^2 \simeq \frac{16\pi^2 \alpha^2 \varepsilon^2}{3} \left(\frac{t}{u} + \frac{u}{t} \right), \quad (\text{B.14})$$

$$I_{12} \simeq \frac{4\pi \alpha^2 \varepsilon^2}{3} [\log(s/m_e^2) - 1]. \quad (\text{B.15})$$

Substituting Eq. (B.15) into Eq. (B.13), we obtain

$$\Gamma_A^{\text{gain}} \simeq -g_1 g_2 g_3 \frac{\alpha^2 \varepsilon^2 T^2}{6\pi \omega p_4} \left[p_4 (1 + \gamma_E - \log T_e) - \frac{\omega_H}{2} \log \frac{2\omega_H}{m_e} + \frac{\omega_L}{2} \log \frac{2\omega_L}{m_e} \right] e^{-\frac{\omega}{T}}, \quad (\text{B.16})$$

where

$$\omega_H = \omega + p_4, \quad \omega_L = \omega - p_4. \quad (\text{B.17})$$

If we neglect $m_{\gamma'}$ such that $\omega_H = 2\omega$ and $\omega_L = 0$, Eq. (B.16) reduces to

$$\Gamma_A^{\text{gain}} \simeq g_1 g_2 g_3 \frac{\alpha^2 \varepsilon^2 T^2 e^{-\omega/T}}{6\pi \omega} \left[\log \left(\frac{4\omega T}{m_e^2} \right) - \gamma_E - 1 \right]. \quad (\text{B.18})$$

Further integrating out the phase space of γ' , we obtain

$$C_A^{\text{gain}} \simeq g_1 g_2 g_3 g_{\gamma'} \frac{\alpha^2 \varepsilon^2 T^4}{6\pi^3} [-\gamma_E + \log(2T_e)]. \quad (\text{B.19})$$

■ Low-temperature limit:

At low temperatures ($T \ll m_e$), I_{12} is approximated as

$$I_{12} \simeq \frac{2\pi \alpha^2 \varepsilon^2}{3} \sqrt{s_e - 4}. \quad (\text{B.20})$$

Substituting it into Eq. (B.13), we obtain

$$\Gamma_A^{\text{gain}} \simeq g_1 g_2 g_3 \frac{\alpha^2 \varepsilon^2 T^{5/2} \omega_H^{3/2}}{24 \sqrt{2} \pi^{1/2} m_e \omega p_4} e^{-\omega/T} \exp \left[-\frac{4m_e^2 - m_{\gamma'}^2}{2\omega_H T} \right]. \quad (\text{B.21})$$

Neglecting the dark photon mass, this reduces to

$$\Gamma_A^{\text{gain}} \simeq g_1 g_2 g_3 \frac{\alpha^2 \varepsilon^2 T^{5/2}}{12 \pi^{1/2} m_e \omega^{1/2}} e^{-\frac{\omega^2 + m_e^2}{\omega T}}. \quad (\text{B.22})$$

The corresponding low- T limit of C_A^{gain} becomes

$$C_A^{\text{gain}} \simeq g_1 g_2 g_3 g_{\gamma'} \frac{\alpha^2 \varepsilon^2 m_e^4 (4T_e^3 + 6T_e^4 + 3T_e^5)}{96 \pi^2} e^{-2m_e/T}. \quad (\text{B.23})$$

B.2 Semi-Compton

The squared amplitude of semi-Compton ($e^- + \gamma \rightarrow e^- + \gamma'$) can be easily obtained using crossing symmetry:

$$|\mathcal{M}_S|^2 = -|\mathcal{M}_A|^2 (t \leftrightarrow s), \quad (\text{B.24})$$

where the subscripts “ S ” and “ A ” indicate semi-Compton and annihilation processes.

The production rate of γ' through this process is given by

$$\Gamma_S^{\text{gain}} \equiv \frac{g_1 g_2 g_3}{2\omega} \int d\Pi_1 d\Pi_2 d\Pi_3 (2\pi\delta)^4 |\mathcal{M}_S|^2 f_1 f_2. \quad (\text{B.25})$$

Since this process may be important when the electron asymmetry becomes significant, we keep the chemical potential of electrons in the calculation. Similar to the calculation for the annihilation process, we first write the integral as

$$\Gamma_S^{\text{gain}} = g_1 g_2 g_3 \frac{e^{\mu_{e^-}/T} e^{-\omega/T}}{2\omega} \int d\Pi_3 e^{-E_3/T} I_{12}, \quad (\text{B.26})$$

with

$$I_{12} = \frac{1}{8\pi \sqrt{\lambda_{s34}}} \int dt |\mathcal{M}_S|^2. \quad (\text{B.27})$$

Due to

$$d\Pi_3 \rightarrow \frac{p_3 ds dp_3}{16\pi^2 p_4 E_3} = \frac{ds dE_3}{16\pi^2 p_4}, \quad (\text{B.28})$$

we rewrite Eq. (B.26) as

$$\Gamma_S^{\text{gain}} = g_1 g_2 g_3 \frac{e^{\mu_{e^-}/T} e^{-\omega/T}}{32\pi^2 \omega p_4} \int dE_3 ds e^{-E_3/T} I_{12}. \quad (\text{B.29})$$

■ High-temperature limit:

At high temperatures ($T \gg m_e$), I_{12} can be approximated as

$$I_{12} \simeq \frac{\pi \alpha^2 \varepsilon^2}{3} \left[1 + 2 \log \left(\frac{s}{m_e^2} \right) \right]. \quad (\text{B.30})$$

Since this is a relatively simple function of s , we choose to first integrate out s and then integrate out E_3 in Eq. (B.29). The integration interval of s , when E_3 is fixed as a given value, is given by

$$s \in m_e^2 + m_{\gamma'}^2 + 2E_3\omega + 2p_3p_4[-1, 1]. \quad (\text{B.31})$$

After integrating out s , we integrate p_3 from 0 to ∞ and obtain

$$\Gamma_S^{\text{gain}} \simeq g_1 g_2 g_3 \frac{\alpha^2 \varepsilon^2 T^2}{24\pi\omega} e^{\mu_{e^-}/T} e^{-\omega/T} \left[2 \log \left(4T_e \frac{\omega}{m_e} \right) - 2\gamma_E + 1 \right]. \quad (\text{B.32})$$

Further integrating out the phase space of γ' , we obtain

$$C_S^{\text{gain}} \simeq g_1 g_2 g_3 g_{\gamma'} \frac{\alpha^2 \varepsilon^2 T^4}{48\pi^3} [3 - 4\gamma_E + 4 \log(2T_e)]. \quad (\text{B.33})$$

■ Low-temperature limit:

At low temperatures when electrons becomes non-relativistic, I_{12} can be approximated as

$$I_{12} \simeq \frac{\pi \alpha^2 \varepsilon^2}{3(s_e - 1)^2 s_e^2} (-1 + 2s_e - 16s_e^2 + 14s_e^3 + s_e^4 + (-6s_e^2 - 12s_e^3 + 2s_e^4) \log s_e), \quad (\text{B.34})$$

where we have neglected the dark photon mass.

Different from the calculation in the high-temperature limit, here we choose to first integrate out E_3 and then integrate out s in Eq. (B.29). The integration intervals of E_3 and s in this integration order are given by

$$E_3 \in [E_3^{\min}, \infty) \quad \text{with} \quad E_3^{\min} \equiv \frac{\omega}{s_e - 1} + m_e^2 \frac{s_e - 1}{4\omega} \quad (\text{B.35})$$

and

$$s \in (m_e^2, \infty). \quad (\text{B.36})$$

First, let us integrate out E_3 :

$$\begin{aligned} \Gamma_S^{\text{gain}} &\simeq g_1 g_2 g_3 \frac{m_e e^{\mu_{e^-}/T} e^{-\omega/T}}{32\pi^2 \omega_e^2} \int ds_e I_{12} \int dE_3 \frac{1}{m_e} e^{-E_3/T} \\ &= g_1 g_2 g_3 \frac{T e^{\mu_{e^-}/T} e^{-\omega/T}}{32\pi^2 \omega_e^2} \int_1^\infty ds_e I_{12} e^{-E_3^{\min}/T}. \end{aligned} \quad (\text{B.37})$$

Next, we integrate out s using the non-relativistic approximation for the final state electron:

$$E_3^{\min} \simeq m_e + m_e^3 \frac{(s_e - 1 - 2\omega/m_e)^2}{8\omega^2}. \quad (\text{B.38})$$

This leads to

$$\Gamma_S^{\text{gain}} \simeq g_1 g_2 g_3 e^{\mu_{e^-}/T} e^{-\frac{\omega+m_e}{T}} \frac{\sqrt{2} \alpha^2 \varepsilon^2 T^{3/2}}{9\sqrt{m_e} \pi^{1/2}}. \quad (\text{B.39})$$

Then it is straightforward to obtain the low- T limit of C_S^{gain} :

$$C_S^{\text{gain}} \simeq g_1 g_2 g_3 g_{\gamma'} e^{\mu_{e^-}/T} e^{-m_e/T} \frac{\sqrt{2} \alpha^2 \varepsilon^2 T^{9/2}}{9\sqrt{m_e} \pi^{5/2}}. \quad (\text{B.40})$$

C The photon self-energy in the thermal bath

In this appendix, we present the calculation of the photon self-energy in the thermal bath of the early Universe during the epoch of $1 \text{ eV} \lesssim T \lesssim 100 \text{ MeV}$. As the temperature decreases, the thermal plasma evolves from the relativistic to the non-relativistic regime, and the electron asymmetry eventually becomes important. The most general formalism to evaluate the photon self-energy, to the leading order in α , reads [44]:

$$\Pi^{\mu\nu} = 16\pi\alpha \int \frac{d^3p}{(2\pi)^3 2E_p} [f_{e^+}(p) + f_{e^-}(p)] \frac{N^{\mu\nu}}{(p \cdot k)^2 - \frac{1}{4}(k \cdot k)^2}, \quad (\text{C.1})$$

with

$$N^{\mu\nu} \equiv (p \cdot k) (p^\mu k^\nu + p^\nu k^\mu) - (k \cdot k) p^\mu p^\nu - g^{\mu\nu} (p \cdot k)^2, \quad (\text{C.2})$$

where k and p denote the photon and electron momenta, respectively. Note that p is an on-shell momentum while k can be off-shell. The phase space distribution functions $f_{e^\pm}(p)$ is given by

$$f_{e^\pm}(p) = \frac{1}{e^{(E_p - \mu_{e^\pm})/T} + 1}. \quad (\text{C.3})$$

Note that $\Pi^{\mu\nu} k_\mu \propto N^{\mu\nu} k_\mu = 0$, allowing us to decompose $\Pi^{\mu\nu}$ as follows

$$\Pi^{\mu\nu} = \Pi_L \epsilon_L^\mu \epsilon_L^\nu + \Pi_T (\epsilon_{T1}^\mu \epsilon_{T1}^\nu + \epsilon_{T2}^\mu \epsilon_{T2}^\nu), \quad (\text{C.4})$$

where ϵ_L and $\epsilon_{T1,2}$ are longitudinal and transverse polarization vectors, satisfying $\epsilon^\mu \epsilon_\mu = -1$ and $k^\mu \epsilon_\mu = 0$. Here and in what follows, we omit the subscripts “ L ” and “ $T1, 2$ ” in identities that apply universally to all the polarization vectors.

In order to extract the Π_L and Π_T components from $\Pi^{\mu\nu}$, we use $\epsilon^\mu \epsilon^\nu$ as a projector since the three polarization vectors are orthonormal, which implies

$$\Pi_L = \Pi_{\mu\nu} \epsilon_L^\mu \epsilon_L^\nu, \quad \Pi_T = \Pi_{\mu\nu} \epsilon_{T1}^\mu \epsilon_{T1}^\nu. \quad (\text{C.5})$$

Multiplying $N^{\mu\nu}$ with the projector, we obtain

$$N_{\mu\nu} \epsilon^\mu \epsilon^\nu = (p \cdot k)^2 - (k \cdot k) (p \cdot \epsilon)^2. \quad (\text{C.6})$$

Without loss of generality, one can assume that k aligns with the z -axis and express all relevant four-vectors as follows:

$$k^\mu = (\omega, 0, 0, k), \quad (\text{C.7})$$

$$p^\mu = (E_p, p s_\theta c_\phi, p s_\theta s_\phi, p c_\theta), \quad (\text{C.8})$$

$$\epsilon_{T1}^\mu = (0, 1, 0, 0), \quad \epsilon_{T2}^\mu = (0, 0, 1, 0), \quad \epsilon_L^\mu = \frac{1}{\sqrt{\omega^2 - k^2}} (k, 0, 0, \omega), \quad (\text{C.9})$$

with $(s_\theta, c_\theta) \equiv (\sin \theta, \cos \theta)$ and $(s_\phi, c_\phi) \equiv (\sin \phi, \cos \phi)$.

Using the explicit forms in Eqs. (C.7)-(C.9), we get

$$p \cdot k = E_p \omega - c_\theta k p,$$

$$p \cdot \epsilon_L = \frac{E_p k - c_\theta p \omega}{\sqrt{\omega^2 - k^2}},$$

$$p \cdot \epsilon_{T1} = -p c_\phi s_\theta.$$

So Eq. (C.6) gives

$$N_{\mu\nu} \epsilon_L^\mu \epsilon_L^\nu = (\omega^2 - k^2) (E_p^2 - c_\theta^2 p^2), \quad (\text{C.10})$$

$$N_{\mu\nu} \epsilon_{T1}^\mu \epsilon_{T1}^\nu = (c_\theta k p - E_p \omega)^2 - c_\phi^2 s_\theta^2 p^2 (\omega^2 - k^2). \quad (\text{C.11})$$

Combining Eq. (C.10) with Eq. (C.1) and neglecting the factor $(k \cdot k)^2$ in the denominator of Eq. (C.1) (see Appendix A.2 in [44]), we obtain

$$\begin{aligned} \Pi_L &= \frac{\alpha}{\pi^2} \int \frac{2\pi p^2 dp dc_\theta}{E_p} (f_{e^+} + f_{e^-}) \frac{(\omega^2 - k^2) (E_p^2 - c_\theta^2 p^2)}{(E_p \omega - c_\theta k p)^2} \\ &= \frac{4\alpha}{\pi} \int \frac{p^2 dp}{E_p} (f_{e^+} + f_{e^-}) \frac{\omega^2 - k^2}{k^2} \left[\frac{\omega}{k v} \log \left(\frac{\omega + k v}{\omega - k v} \right) - \frac{\omega^2 - k^2}{\omega^2 - k^2 v^2} - 1 \right], \end{aligned} \quad (\text{C.12})$$

where $v \equiv p/E_p$.

Combining Eq. (C.11) with Eq. (C.1), we obtain

$$\begin{aligned} \Pi_T &= \frac{\alpha}{\pi^2} \int \frac{p^2 dp d\Omega}{E_p} (f_{e^+} + f_{e^-}) \frac{(c_\theta k p - E_p \omega)^2 - c_\phi^2 s_\theta^2 p^2 (\omega^2 - k^2)}{(E_p \omega - c_\theta k p)^2} \\ &= \frac{4\alpha}{\pi} \int \frac{p^2 dp}{E_p} (f_{e^+} + f_{e^-}) \left[\frac{\omega^2}{k^2} - \frac{\omega^2 - k^2}{k^2} \cdot \frac{\omega}{2k v} \log \left(\frac{\omega + k v}{\omega - k v} \right) \right]. \end{aligned} \quad (\text{C.13})$$

Eqs. (C.12) and (C.13) are ready for straightforward numerical evaluation. Nevertheless, it is worth mentioning the relativistic and nonrelativistic limits of Π_L and Π_T .

When f_{e^\pm} are nonrelativistic, we replace $\int p^2 dp f_{e^\pm} \rightarrow \pi^2 n_{e^\pm}$ and take $v \rightarrow 0$ in Eqs. (C.12) and (C.13). The resulting nonrelativistic limits are

$$\Pi_T \approx 4\pi\alpha \frac{n_{e^+} + n_{e^-}}{m_e}, \quad (\text{C.14})$$

$$\Pi_L \approx 4\pi\alpha \frac{n_{e^+} + n_{e^-}}{m_e} \left(1 - \frac{k^2}{\omega^2} \right). \quad (\text{C.15})$$

When f_{e^\pm} are relativistic, we neglect the electron mass (hence $v \rightarrow 1$) and the chemical potential. This allows us to replace $\int \frac{p^2}{E_p} dp f_{e^\pm} \rightarrow \pi^2 T^2/6$. The resulting relativistic limits are

$$\Pi_T \approx \frac{2\pi\alpha T^2}{3} \left(\frac{\omega^2}{k^2} - \frac{\omega}{2k} \frac{\omega^2 - k^2}{k^2} \log \left(\frac{\omega + k}{\omega - k} \right) \right), \quad (\text{C.16})$$

$$\Pi_L \approx \frac{2}{3} \pi\alpha T^2 \left(\frac{\omega^2}{k^2} - 1 \right) \left(\frac{\omega}{k} \log \left(\frac{\omega + k}{\omega - k} \right) - 2 \right). \quad (\text{C.17})$$

For $k \ll \omega$, they reduce to

$$\Pi_T \approx \Pi_L \approx \frac{4\pi\alpha}{9} T^2. \quad (\text{C.18})$$

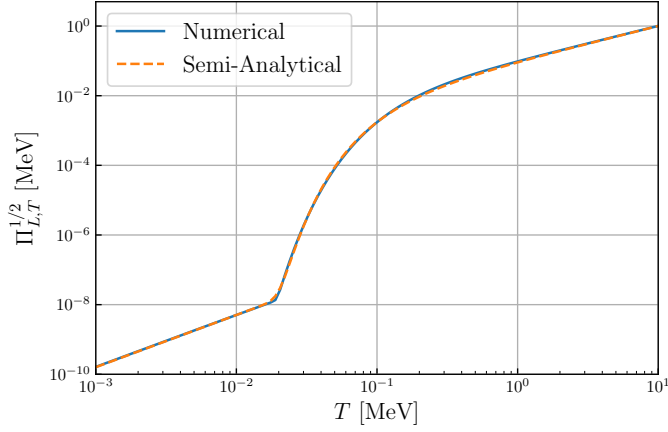


Figure 7. Numerical evaluation of $\Pi_{T,L}$ compared with the our semi-analytical expression given by Eqs. (C.19) and (C.20).

Therefore it is convenient to parametrized $\Pi_{T,L}$ as follows:

$$\Pi_{T,L} = \frac{4\pi\alpha}{9} T^2 F_{T,L}^2, \quad (\text{C.19})$$

where $F_{T,L}$ accounts for the deviation of $\Pi_{T,L}$ from their relativistic limit. By integrating Eqs. (C.12) and (C.13) numerically, we can obtain $\Pi_{T,L}$ and extract $F_{T,L}$ from it. In practice, we find that the following expression can fit the numerical values very accurately:

$$F_{T,L} \approx 5 \times 10^{-5} \sqrt{x} + \exp\left(-\frac{x^{-6/5}}{9}\right), \quad (\text{C.20})$$

with $x \equiv T/\text{MeV}$. Figure 7 shows the accuracy of the above expression in comparison with the numerical results.

References

- [1] B. Holdom, *Two $U(1)$'s and Epsilon Charge Shifts*, *Phys. Lett. B* **166** (1986) 196–198.
- [2] J. Jaeckel and A. Ringwald, *The Low-Energy Frontier of Particle Physics*, *Ann. Rev. Nucl. Part. Sci.* **60** (2010) 405–437, [[1002.0329](#)].
- [3] R. Essig *et al.*, *Working Group Report: New Light Weakly Coupled Particles*, in *Community Summer Study 2013: Snowmass on the Mississippi*, 10, 2013. [[1311.0029](#)].
- [4] J. Alexander *et al.*, *Dark Sectors 2016 Workshop: Community Report*, 8, 2016. [[1608.08632](#)].
- [5] P. Ilten, Y. Soreq, M. Williams, and W. Xue, *Serendipity in dark photon searches*, *JHEP* **06** (2018) 004, [[1801.04847](#)].
- [6] M. Bauer, P. Foldenauer, and J. Jaeckel, *Hunting All the Hidden Photons*, *JHEP* **18** (2020) 094, [[1803.05466](#)].
- [7] M. Fabbrichesi, E. Gabrielli, and G. Lanfranchi, *The Dark Photon*, [[2005.01515](#)].

- [8] A. Caputo, A. J. Millar, C. A. J. O'Hare, and E. Vitagliano, *Dark photon limits: A handbook*, *Phys. Rev. D* **104** (2021), no. 9 095029, [[2105.04565](#)].
- [9] **Belle-II Collaboration**, F. Abudinén *et al.*, *Search for a Dark Photon and an Invisible Dark Higgs Boson in $\mu+\mu^-$ and Missing Energy Final States with the Belle II Experiment*, *Phys. Rev. Lett.* **130** (2023), no. 7 071804, [[2207.00509](#)].
- [10] J. L. Feng, I. Galon, F. Kling, and S. Trojanowski, *ForwArd Search ExpeRiment at the LHC*, *Phys. Rev. D* **97** (2018), no. 3 035001, [[1708.09389](#)].
- [11] **FASER Collaboration**, H. Abreu *et al.*, *First Direct Observation of Collider Neutrinos with FASER at the LHC*, [2303.14185](#).
- [12] S. Alekhin *et al.*, *A facility to Search for Hidden Particles at the CERN SPS: the SHiP physics case*, *Rept. Prog. Phys.* **79** (2016), no. 12 124201, [[1504.04855](#)].
- [13] S. Gardner, R. J. Holt, and A. S. Tadepalli, *New Prospects in Fixed Target Searches for Dark Forces with the SeaQuest Experiment at Fermilab*, *Phys. Rev. D* **93** (2016), no. 11 115015, [[1509.00050](#)].
- [14] A. Berlin, S. Gori, P. Schuster, and N. Toro, *Dark Sectors at the Fermilab SeaQuest Experiment*, *Phys. Rev. D* **98** (2018), no. 3 035011, [[1804.00661](#)].
- [15] J. P. Chou, D. Curtin, and H. J. Lubatti, *New Detectors to Explore the Lifetime Frontier*, *Phys. Lett. B* **767** (2017) 29–36, [[1606.06298](#)].
- [16] **MATHUSLA Collaboration**, C. Alpigiani *et al.*, *An Update to the Letter of Intent for MATHUSLA: Search for Long-Lived Particles at the HL-LHC*, [2009.01693](#).
- [17] J. Redondo and M. Postma, *Massive hidden photons as lukewarm dark matter*, *JCAP* **02** (2009) 005, [[0811.0326](#)].
- [18] A. Fradette, M. Pospelov, J. Pradler, and A. Ritz, *Cosmological Constraints on Very Dark Photons*, *Phys. Rev. D* **90** (2014), no. 3 035022, [[1407.0993](#)].
- [19] J. Berger, K. Jedamzik, and D. G. E. Walker, *Cosmological Constraints on Decoupled Dark Photons and Dark Higgs*, *JCAP* **11** (2016) 032, [[1605.07195](#)].
- [20] M. Pospelov, J. Pradler, J. T. Ruderman, and A. Urbano, *Room for New Physics in the Rayleigh-Jeans Tail of the Cosmic Microwave Background*, *Phys. Rev. Lett.* **121** (2018), no. 3 031103, [[1803.07048](#)].
- [21] M. Ibe, S. Kobayashi, Y. Nakayama, and S. Shirai, *Cosmological constraint on dark photon from N_{eff}* , *JHEP* **04** (2020) 009, [[1912.12152](#)].
- [22] S. D. McDermott and S. J. Witte, *Cosmological evolution of light dark photon dark matter*, *Phys. Rev. D* **101** (2020), no. 6 063030, [[1911.05086](#)].
- [23] J. Coffey, L. Forestell, D. E. Morrissey, and G. White, *Cosmological Bounds on sub-GeV Dark Vector Bosons from Electromagnetic Energy Injection*, *JHEP* **07** (2020) 179, [[2003.02273](#)].
- [24] J.-T. Li, G. M. Fuller, and E. Grohs, *Probing dark photons in the early universe with big bang nucleosynthesis*, *JCAP* **12** (2020) 049, [[2009.14325](#)].
- [25] A. Caputo, H. Liu, S. Mishra-Sharma, M. Pospelov, and J. T. Ruderman, *Radio excess from stimulated dark matter decay*, *Phys. Rev. D* **107** (2023), no. 12 123033, [[2206.07713](#)].
- [26] D. Pîrvu, J. Huang, and M. C. Johnson, *Patchy screening of the CMB from dark photons*, *JCAP* **01** (2024) 019, [[2307.15124](#)].

- [27] X. Gan and D. Liu, *Cosmologically varying kinetic mixing*, *JHEP* **11** (2023) 031, [[2302.03056](#)].
- [28] D. Cyncynates and Z. J. Weiner, *Detectable and Defect-Free Dark Photon Dark Matter*, *Phys. Rev. Lett.* **134** (2025), no. 21 211002, [[2310.18397](#)].
- [29] A. Aramburo-Garcia, K. Bondarenko, A. Boyarsky, P. Kashko, J. Pradler, A. Sokolenko, R. Kugel, M. Schaller, and J. Schaye, *Dark photon constraints from CMB temperature anisotropies*, *JCAP* **11** (2024) 049, [[2405.05104](#)].
- [30] F. McCarthy, D. Pirvu, J. C. Hill, J. Huang, M. C. Johnson, and K. K. Rogers, *Dark Photon Limits from Patchy Dark Screening of the Cosmic Microwave Background*, *Phys. Rev. Lett.* **133** (2024), no. 14 141003, [[2406.02546](#)].
- [31] A. Trost, J. S. Bolton, A. Caputo, H. Liu, S. Cristiani, and M. Viel, *Constraints on dark photon dark matter from Lyman- α forest simulations and an ultrahigh signal-to-noise quasar spectrum*, *Phys. Rev. D* **111** (2025), no. 8 083034, [[2410.02858](#)].
- [32] D. Cyncynates and Z. J. Weiner, *Experimental targets for dark photon dark matter*, *Phys. Rev. D* **111** (2025), no. 10 103535, [[2410.14774](#)].
- [33] A. Hook, J. Huang, and M. Shalaby, *No cosmological constraints on dark photon dark matter from resonant conversion: Impact of nonlinear plasma dynamics*, [2510.13956](#).
- [34] M. Lindner, F. S. Queiroz, W. Rodejohann, and X.-J. Xu, *Neutrino-electron scattering: general constraints on Z' and dark photon models*, *JHEP* **05** (2018) 098, [[1803.00060](#)].
- [35] S.-P. Li and X.-J. Xu, *Production rates of dark photons and Z' in the Sun and stellar cooling bounds*, *JCAP* **09** (2023) 009, [[2304.12907](#)].
- [36] E. C. G. Stueckelberg, *Interaction energy in electrodynamics and in the field theory of nuclear forces*, *Helv. Phys. Acta* **11** (1938) 225–244.
- [37] D. Feldman, Z. Liu, and P. Nath, *The Stueckelberg Z' -prime Extension with Kinetic Mixing and Milli-Charged Dark Matter From the Hidden Sector*, *Phys. Rev. D* **75** (2007) 115001, [[hep-ph/0702123](#)].
- [38] S.-P. Li and X.-J. Xu, *Dark matter produced from right-handed neutrinos*, *JCAP* **06** (2023) 047, [[2212.09109](#)].
- [39] X. Luo, W. Rodejohann, and X.-J. Xu, *Dirac neutrinos and N_{eff} . Part II. The freeze-in case*, *JCAP* **03** (2021) 082, [[2011.13059](#)].
- [40] C. O’Hare, “cajohare/axionlimits: Axionlimits.” <https://cajohare.github.io/AxionLimits/>, July, 2020.
- [41] J. Redondo, *Helioscope Bounds on Hidden Sector Photons*, *JCAP* **07** (2008) 008, [[0801.1527](#)].
- [42] H. An, M. Pospelov, and J. Pradler, *New stellar constraints on dark photons*, *Phys. Lett. B* **725** (2013) 190–195, [[1302.3884](#)].
- [43] J. Redondo and G. Raffelt, *Solar constraints on hidden photons re-visited*, *JCAP* **08** (2013) 034, [[1305.2920](#)].
- [44] E. Braaten and D. Segel, *Neutrino energy loss from the plasma process at all temperatures and densities*, *Phys. Rev. D* **48** (1993) 1478–1491, [[hep-ph/9302213](#)].
- [45] H. A. Weldon, *Simple Rules for Discontinuities in Finite Temperature Field Theory*, *Phys. Rev. D* **28** (1983) 2007.

- [46] L. Wolfenstein, *Neutrino Oscillations in Matter*, *Phys.Rev.* **D17** (1978) 2369–2374.
- [47] S. P. Mikheev and A. Yu. Smirnov, *Resonance Amplification of Oscillations in Matter and Spectroscopy of Solar Neutrinos*, *Sov. J. Nucl. Phys.* **42** (1985) 913–917. [*Yad. Fiz.*42,1441(1985)].
- [48] S. P. Mikheev and A. Yu. Smirnov, *Resonant amplification of neutrino oscillations in matter and solar neutrino spectroscopy*, *Nuovo Cim.* **C9** (1986) 17–26.
- [49] Q.-f. Wu and X.-J. Xu, *A comprehensive calculation of the Primakoff process and the solar axion flux*, *JCAP* **07** (2024) 013, [[2402.16083](#)].
- [50] M. Pospelov, A. Ritz, and M. B. Voloshin, *Bosonic super-WIMPs as keV-scale dark matter*, *Phys. Rev. D* **78** (2008) 115012, [[0807.3279](#)].
- [51] S. D. McDermott, H. H. Patel, and H. Ramani, *Dark Photon Decay Beyond The Euler-Heisenberg Limit*, *Phys. Rev. D* **97** (2018), no. 7 073005, [[1705.00619](#)].
- [52] T. Linden, T. T. Q. Nguyen, and T. M. P. Tait, *Indirect Searches for Dark Photon-Photon Tridents in Celestial Objects*, [2402.01839](#).
- [53] T. Linden, T. T. Q. Nguyen, and T. M. P. Tait, *X-Ray Constraints on Dark Photon Tridents*, [2406.19445](#).
- [54] **Particle Data Group Collaboration**, S. Navas *et al.*, *Review of particle physics*, *Phys. Rev. D* **110** (2024), no. 3 030001.
- [55] **Planck Collaboration**, N. Aghanim *et al.*, *Planck 2018 results. VI. Cosmological parameters*, *Astron. Astrophys.* **641** (2020) A6, [[1807.06209](#)]. [Erratum: *Astron.Astrophys.* 652, C4 (2021)].
- [56] S.-P. Li and X.-J. Xu, *N_{eff} constraints on light mediators coupled to neutrinos: the dilution-resistant effect*, *JHEP* **10** (2023) 012, [[2307.13967](#)].
- [57] M. Kawasaki, K. Kohri, T. Moroi, and Y. Takaesu, *Revisiting Big-Bang Nucleosynthesis Constraints on Long-Lived Decaying Particles*, *Phys. Rev. D* **97** (2018), no. 2 023502, [[1709.01211](#)].
- [58] M. Hufnagel, K. Schmidt-Hoberg, and S. Wild, *BBN constraints on MeV-scale dark sectors. Part II. Electromagnetic decays*, *JCAP* **11** (2018) 032, [[1808.09324](#)].
- [59] L. Forestell, D. E. Morrissey, and G. White, *Limits from BBN on Light Electromagnetic Decays*, *JHEP* **01** (2019) 074, [[1809.01179](#)].
- [60] W. Hu and J. Silk, *Thermalization constraints and spectral distortions for massive unstable relic particles*, *Phys. Rev. Lett.* **70** (1993) 2661–2664.
- [61] J. Chluba and R. A. Sunyaev, *The evolution of CMB spectral distortions in the early Universe*, *Mon. Not. Roy. Astron. Soc.* **419** (2012) 1294–1314, [[1109.6552](#)].
- [62] V. Poulin, J. Lesgourgues, and P. D. Serpico, *Cosmological constraints on exotic injection of electromagnetic energy*, *JCAP* **03** (2017) 043, [[1610.10051](#)].
- [63] J. H. Chang, R. Essig, and S. D. McDermott, *Revisiting Supernova 1987A Constraints on Dark Photons*, *JHEP* **01** (2017) 107, [[1611.03864](#)].
- [64] A. Caputo, J. Park, and S. Yun, *The Heavy Dark Photon Handbook: Cosmological and Astrophysical Bounds*, [2511.15785](#).

- [65] X. Luo, W. Rodejohann, and X.-J. Xu, *Dirac neutrinos and N_{eff}* , *JCAP* **06** (2020) 058, [[2005.01629](#)].